POLYmer based electro-optic PCB motherboard integration with Si_3N_4 Chiplets, InP Components and Electronic ICs enabling affordable photonic modules for THz Sensing and quantum computing applications

Deliverable D2.6

Final report on system and components specifications and system simulations

Lead Beneficiary	ICCS
Contact Person	Prof. Hercules Avramopoulos
Address	9 Iroon Polytechniou Str., 15780 Athens, Greece
Phone	+30 210 772 2076
e-mail	hav@mail.ntua.gr

Date due of deliverable	30.04.2025 (M28)
Actual submission date	11.08.2025
Authors	C.Tsokos, E. Loukisa, S. Paraskevopoulou
Participants	TOPTICA, QuiX, LioniX

Work-package	WP2
Dissemination level	PU - Public
Type	R – Document, report
Version	1.0
Total number of pages	58

POLYNICES | HORIZON-RIA
HORIZON-CL4-2021-DIGITAL EMERGING-01-07
Project no.: 101070549
Start Date: 1 January 2023
Duration: 42 Months

Funded by the European Union

Document History

Version	Date dd.mm.yy	From > To	Description
0.1	01.03.2025	ICCS	Update on POLYNICES functional layouts
0.2	30.06.2025	ICCS	Update on simulation studies
0.3	05.08.2025	QuiX, LXI > ICCS	Update on Functional Layout of Demo-2B
1.0	11.08.2025	ICCS	Final revision and submission

TABLE OF CONTENTS

List of abbreviations

AC	Alternating current
ADS	Asymmetric double stripe
BW	Bandwidth
CI	Carrier insertion
CM	Clements matrix
DC	Direct current
DRW	Dielectric rod waveguide
EC	European Commission
ECL	External cavity laser
EDFA	Erbium-doped fiber amplifier
EOPCB	Electro-optic printed circuit board
FA	Fiber array
FMCW	Frequency modulated continuous wave
FSPL	Free-space path losses
FSR	Free spectral range
GRIN	Gradient index
HF	High-frequency
IC	Integrated circuit
IF	Intermediate frequency
InP	Indium phosphide
KPI	Key performance indicators
KTP	Potassium titanyl phosphate
LO	Local oscillator
MRR	Micro-ring resonator
MZI	Mach-Zehnder interferometer
NDT	Non-destructive testing
OBFN	Optical beamforming network
PBS	Polarization beam splitter
PC	Polarization controller
PCA	Photoconductive antenna
PCB	Printed circuit board
PD	Photodiode
PIC	Photonic integrated circuit
PM	Polarization-maintaining
ppKTP	Periodic poled potassium titanyl phosphate
PR	Polarization rotator
PS	Phase shifter
PZT	Lead Zirconate Titanate

QIP	Quantum information processor
RAMZI	Ring-assisted Mach-Zehnder interferometer
RIN	Relative intensity noise
RSOA	Reflective semiconductor optical amplifier
S-DSH	Swept-delayed self-heterodyning
SMF	Single-mode fiber
SOA	Semiconductor optical amplifier
TBS	Tunable beam splitter
TDS	Time-domain spectroscopy
TIA	Transimpedance amplifier
TMM	Transfer matrix method
WP	Work package

Executive Summary

Deliverable D2.6 presents the final set of system and component specifications, defined by the requirements arising from the targeted application scenarios and the results of system simulation studies.

The first part of the deliverable addresses the functional designs of the POLYNICES prototypes. Over the course of the project, two fully integrated optoelectronic Frequency Modulated Continuous Wave (FMCW) Terahertz (THz) spectrometers will be developed. **Demo-1A** will be a single-channel FMCW THz spectrometer, while **Demo-1B** will support multi-channel operation with beamforming capabilities. In preparation for these final prototypes, three precursors—**Precursor-0A**, **Precursor-1A**, and **Precursor-1B**—have been created to validate testing methodologies for individual components and to provide essential feedback for design and fabrication. The functional designs for all prototypes have been carefully derived in accordance with the system requirements set out in Deliverable D2.1.

In parallel with the spectrometer developments, the POLYNICES project is advancing a series of quantum information processors that integrate on-PIC components Mach–Zehnder interferometer matrices based on the Clements architecture. **Precursor-2A** consists of a fiber-pigtailed ppKTP crystal assembly, incorporating gradient-index microlenses and polarization-handling elements. This will lead to **Demo-2A**, an 8×8 quantum information processor using a 775 nm laser source, four ppKTP crystals, and an 8×8 Clements matrix. The final iteration, **Demo-2B**, will employ a 1550 nm laser source, micro-ring resonators, and an 8×8 Clements matrix, marking the culmination of the quantum information processing system.

The second and final part of this deliverable presents the updated system simulations, with a particular focus on assessing the noise performance of the FMCW THz spectrometer and refining the calibration methods for the Clements matrices.

Keywords: Functional designs, system specifications, system simulations, FMCW THz spectrometer, Blass-matrix based optical beamforming network, quantum information processor, Clements matrix

1 INTRODUCTION

POLYNICES is a research and innovation initiative aimed at delivering a versatile photonic integration platform that combines cost-effectiveness, high performance, scalability, and manufacturability—key attributes for enabling the next generation of photonic modules. The project introduces an innovative approach by applying Fraunhofer's polymer photonic platform, known as **PolyBoard**, onto printed circuit boards (PCBs) via a spin-coating process. This technique enables the fabrication of cost-efficient Electro-Optic PCB (EOPCB) motherboards with low-loss single-mode waveguides and favorable high-frequency (HF) properties.

The EOPCB serves as a host platform for **silicon nitride**, based on LioniX's proprietary TriPleX photonic platform, and for **Indium Phosphide (InP) chiplets**, enabling advanced functionalities. Its advantageous HF performance further supports the direct integration of terahertz (THz) antennas. Using these core building blocks, POLYNICES will develop two families of prototypes, each targeting distinct application domains.

This deliverable presents the final set of system and component specifications, derived from the requirements established in Deliverable D2.1 "*Use Cases, System Requirements, and KPIs of POLYNICES Demonstrators*", and builds upon the initial system simulations reported in Deliverable D2.2 "*Initial Report on System and Components Specifications and System Simulations*".

Chapter 2 details the functional designs of all prototypes, outlining their intended functionalities and key building blocks. Chapter 3 presents the system simulation studies for both prototype families. For the FMCW THz spectrometer prototypes, the analysis evaluates the impact of component-induced noise by calculating the power spectral density for different noise sources at multiple points in the system, along with the signal-to-noise ratio at the receiver. In addition, the chapter reports on the development of calibration methods for the Blass matrix-based optical beamforming networks—integral to Precursor-1B and Demo-1B—and for the Clements matrices used in Demo-2A and Demo-2B.

2 FUNCTIONAL DESIGNS OF POLYNICES PROTOTYPES

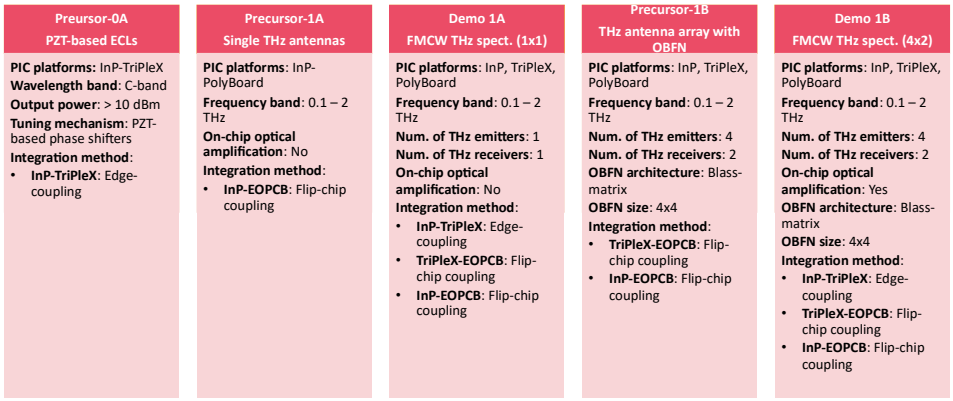

Figure 1. Summary of the modules for the application of the THz spectrometer. Demo 1A and 1B as demonstrators for the POLYNICES technology and the three precursor modules (Precursor-0A, Precursor-1A, and Precursor-1B).

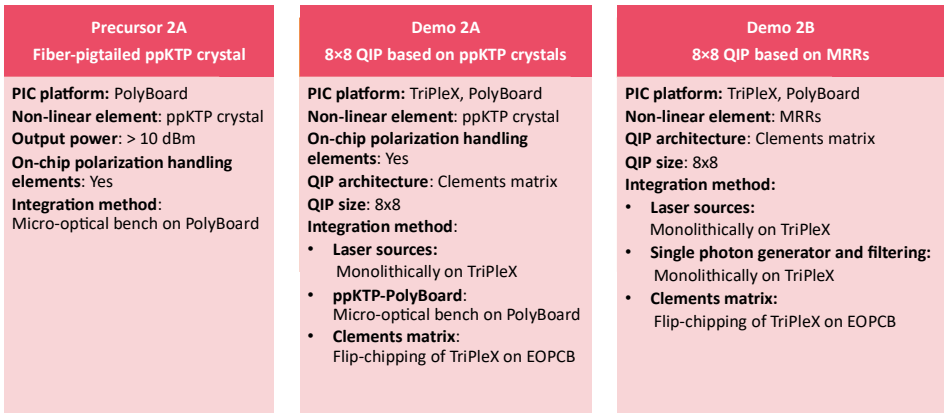

Figure 2. Summary of the quantum information processors prototypes that will be developed in POLYNICES.

As reported in deliverable D2.1 "*Use cases, system requirements and KPIs of POLYNICES demonstrators*" during the course of POLYNICES project two fully integrated optoelectronics FMCW THz spectrometers will be developed. **Demo-1A** will be a single-channel FMWC THz spectrometer while **Demo-1B** will support a multi-channel operation with beamforming capabilities. In addition to the proposed Demo-1A and Demo-1B, three precursors (**Precursor-0A, Precursor-1A and Precursor-1B**) have been included in order to validate the testing methodologies of the individual components of the final prototypes and more importantly, to provide useful feedback on the design and fabrication activities. Figure 1and Figure 2 provide an overview of the respective planned modules and the components on the boards. As observed, the integration complexity as well as the number of supported functionalities increases as you move to the right-hand side.

2.1 Precursor-0A: PZT-based external cavity laser sources

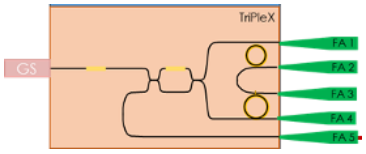

Figure 3. Functional layout of Precuros-0A

Precursor-0A represents the foundational laser source developed for use in terahertz (THz) photonic integrated circuit (PIC) systems It generates an independent optical carrier spanning the entire C-band. Two Precursor-0A will be fabricated each capable of stable, narrow-linewidth, high-power emission. Each ECL uses an InP-based reflective semiconductor optical amplifier (RSOA) as its gain medium.

These RSOAs are edge-coupled to a silicon nitride (Si_3N_4, TriPleX) waveguide circuit that acts as the external optical cavity. This hybrid approach leverages the superior gain properties of InP with the low-loss and high-Q characteristics of TriPleX passive components. The coupling strategy ensures efficient optical feedback and low insertion loss, which is critical for maintaining high optical performance.

The external cavity design integrates two coupled micro-ring resonators (MRRs) with slightly different free spectral ranges (FSRs). This configuration exploits the Vernier effect to ensure stable single-mode lasing operation by selectively reinforcing only one wavelength across the gain bandwidth. Additionally, the cavity includes two Mach–Zehnder interferometers (MZIs), which are arranged in a loop mirror configuration. The combination of MRRs and MZIs enables wavelength-selective optical feedback to both gain sections of each ECL. This feedback loop is vital for achieving the high coherence and spectral purity required for downstream THz applications.

Due to the exceptionally low propagation loss of approximately 0.1 dB/cm in the TriPleX waveguide and the extended cavity length, Precursor-0A achieves a narrow optical linewidth of less than 1 kHz. This level of performance is particularly important for applications involving high-frequency signal generation, where phase noise and linewidth directly impact system stability and resolution. Moreover, the ECLs are equipped with integrated piezoelectric transducer (PZT) phase shifters that provide fine-tuning capabilities. These PZT shifters support tuning speeds in the MHz range, allowing rapid wavelength adjustments to accommodate dynamic system requirements or environmental drift.

Each ECL is designed to deliver more than 10 dBm of optical output power, constrained primarily by the saturation characteristics of the selected RSOAs. The single-section design simplifies system integration and contributes to overall power efficiency. The optical outputs are connected to a polarization-maintaining (PM) fiber array, ensuring stable coupling and alignment with subsequent modules in the THz generation or detection chain.

To facilitate calibration and monitoring during system assembly and operation, Precursor-0A includes dedicated optical monitoring ports. These ports are integrated into the circuit layout and enable real-time observation of the ECL behavior, making it easier to adjust tuning, stabilize outputs, and ensure precise spectral alignment between the two laser sources.

2.2 Precursor-1A: Single THz antennas

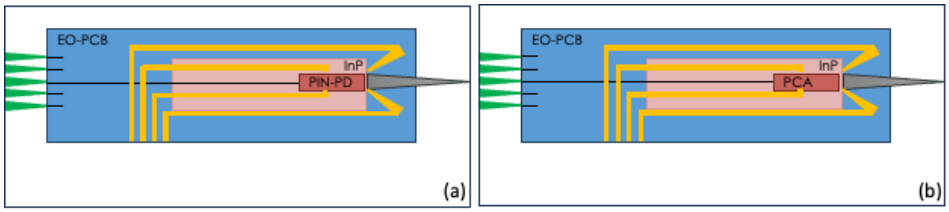

Figure 4. Functional designs of the (a) transmitter and (b) receiver of Precursor-1A.

Within the POLYNICES project, the generation and detection of terahertz (THz) signals will rely on a hybrid integration approach that combines a thin silicon rod antenna with InP-based optoelectronic components. Specifically, signal emission will be facilitated by an InP PIN photodiode (PD), while detection will be performed by an InP photoconductive element. The architectural and functional designs for both the THz transmitter and receiver in Precursor-1A are illustrated in Figure 4. Unlike Precursor-0A, which focused solely on high-power optical sources, Precursor-1A represents the first prototype developed using the POLYNICES integration strategy. This approach involves the use of an electro-optic printed circuit board (EOPCB) that accommodates both the InP photonic devices and the silicon rod antennas on a unified platform.

Precursor-1A is being designed to support operation at THz frequencies exceeding 1 THz. However, based on the high-frequency characteristics of the InP photonic components and the electromagnetic behavior of the silicon rod antennas, the system shows strong potential for signal generation and detection at frequencies approaching 2 THz. This extended operational range highlights the scalability and versatility of the POLYNICES integration concept.

On the transmission side, the InP PIN photodiode will be optically driven via a single polarization-maintaining (PM) fiber, which delivers the input optical signal. To generate THz signals through photomixing, the optical input must consist of two carriers with a frequency spacing equal to the desired THz output frequency. In the case of Precursor-1A, the input will include one unmodulated optical carrier with a fixed central wavelength and a second, rapidly frequency-swept signal. This optical configuration enables frequency-tunable THz generation.

To ensure the safe and reliable operation of the InP PIN-PD, the input optical power will be limited to a maximum of 15 dBm. Furthermore, due to the inherent polarization dependence of the InP platform—optimized for transverse electric (TE) mode—the optical input must be strictly TE-polarized. This requirement is fulfilled by using PM fibers for optical delivery and integrating external polarization controllers at the fiber inputs. These polarization controllers will maintain the required TE polarization state regardless of any system-level perturbations.

The same input signal characteristics and polarization constraints apply to the receiver subsystem. However, in this case, the InP PIN photodiode is replaced with an InP-based photoconductive element that performs optical-to-THz signal conversion for detection purposes. This symmetry between the transmitter and receiver designs simplifies alignment and integration while allowing full system validation across a wide THz frequency range.

2.3 Demo-1A: Single channel FMCW THz spectrometer

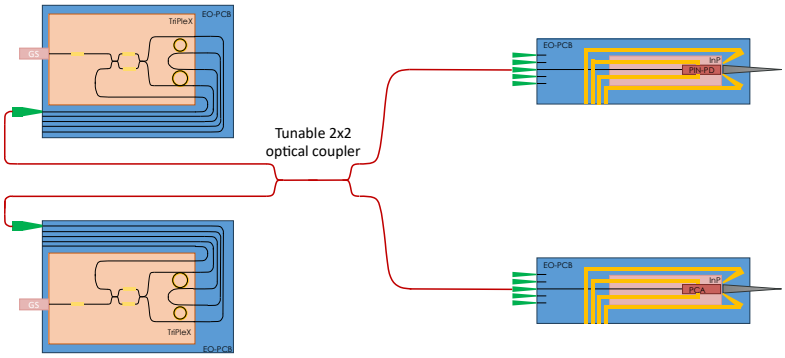

Figure 5. Functional design of Demo-1A.

Demo-1A will be the first fully developed prototype in the POLYNICES project under the category of FMCW THz spectrometers. It represents a key milestone in the project's progression and is designed as a **single-channel system** dedicated to **non-destructive thickness measurement** applications. Figure 5 shows the updated and more detailed functional design of this prototype, illustrating the architecture and integration approach.

Demo-1A will be built on the POLYNICES **electro-optic printed circuit board (EOPCB)** platform, using **PolyBoard** as the base motherboard. Onto this platform, **TriPleX and InP photonic integrated circuits (PICs)** will be mounted using **flip-chip bonding**. For clarity in Figure 5, the TriPleX and InP chips are shown prior to the bonding process, with their active sides facing upward. After flip-chipping, the backside of the chips will be aligned flush with the top surface of the PolyBoard, enabling seamless electrical and optical interfacing.

From a system functionality standpoint, Demo-1A incorporates two primary functions, along with an additional feature dedicated to optical monitoring and feedback.

The first key function is the **generation of dual optical signals** that are required for THz signal production. Demo-1A will rely on **two external cavity laser sources** developed by LioniX. One laser will produce a stable optical carrier with a fixed central frequency, while the second will generate a **frequency-modulated continuous wave (FMCW)** signal. To produce THz signals up to 2 THz, the modulated laser must rapidly sweep across a 16 nm span within the C-band at a tuning speed of 500 THz per second. This modulation is made possible through the use of thermo-optic phase shifters, which will control the optical path length within the cavity. While the cavity of the unmodulated laser remains fixed during operation, the dynamic sweeping of the FMCW source is essential for achieving the desired high-frequency output. The behavior of these laser sources will be experimentally evaluated using **Precursor-0A**, which includes the exact same ECL configurations and provides a test platform for their calibration and fine-tuning.

The second main function focuses on the **transmission and reception of the generated THz signals**. Echoing the architecture of **Precursor-1A**, Demo-1A will use a transmitter composed of an **InP PIN photodiode (PIN-PD)** paired with a **silicon rod antenna**, and a receiver consisting of an **InP photoconductive element (PCA)** also coupled with a silicon rod antenna. This setup enables efficient optical-to-THz and THz-to-electrical signal conversion. To minimize channel interference, the transmitter and receiver modules will be separated by a distance of over 4 millimeters, which is sufficient to reduce crosstalk to approximately −35 dB. Additional suppression of unwanted interference can be achieved by inserting THz-absorbing materials between the two modules during final assembly.

2.4 Precursor-1B: THz antenna array with beamforming capabilities

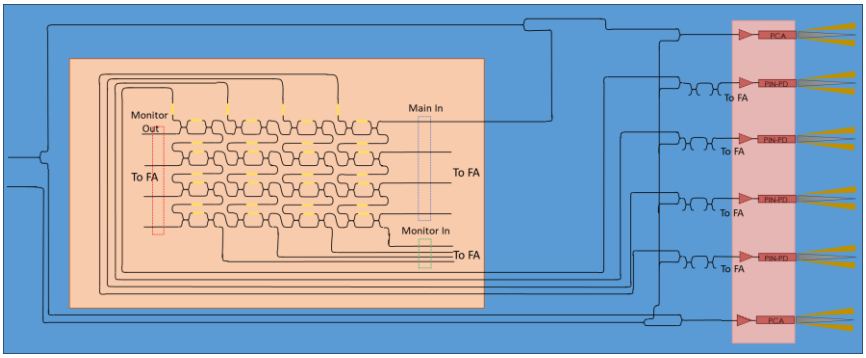

Figure 6. Functional design of Precursor-1B.

Precursor-1B will introduce a significant advancement in the POLYNICES project by integrating a **4×4 optical beamforming network (OBFN)** based on the **Blass matrix architecture**, coupled with a **carrier insertion (CI) stage**, and an array of **four THz transmitters and two THz receivers**. This prototype marks the first implementation of an OBFN directly interfaced with THz antennas on the POLYNICES electro-optic printed circuit board (EOPCB), demonstrating the full capabilities of the platform's hybrid integration approach. The functional design of Precursor-1B is illustrated in Figure 6.

At the core of the system lies the 4×4 Blass matrix OBFN, which consists of four horizontal and four vertical optical waveguides. These are interconnected through multiple **Mach–Zehnder interferometers (MZIs)**, which allow each input signal to be split into several paths and routed through the network. The MZIs enable precise phase control, allowing signals from different input ports to be recombined coherently and directed to specific output ports. This configuration supports the formation of up to **four independent THz beams**, each corresponding to one of the four antenna elements in the array.

Precursor-1B will be driven by two optical inputs: one **static optical carrier** with a fixed central wavelength and one **FMCW optical signal** with a sweeping frequency across the C-band. The static carrier is injected into the first input of the Blass matrix, where it is divided into four branches. At the output of the OBFN, each signal will carry a specific relative phase difference. This phase difference is determined by both the desired beam steering angle and the instantaneous frequency of the THz signal being generated.

In parallel, the frequency-swept FMCW signal is routed into the **carrier insertion (CI) stage**, which is constructed from a cascade of six MZIs. The CI stage serves different roles for the transmitter and receiver paths. On the **transmitter side**, it combines the four OBFN outputs (derived from the static carrier) with the FMCW signal, producing the required **dual-optical input** needed to generate a THz FMCW signal via photomixing. On the **receiver side**, the CI stage combines the FMCW signal with the static optical signal that bypasses the OBFN. This configuration ensures coherent detection at each receiver channel.

As with Precursor-1A and Demo-1A, the THz transmitter and receiver arrays will be based on the integration of **InP PIN photodiodes (PIN-PDs)** and **photoconductive antennas (PCAs)** with **thin silicon rod antennas**. However, a key enhancement in Precursor-1B is the inclusion of **semiconductor optical amplifiers (SOAs)**. These SOAs are incorporated to compensate for optical losses due to waveguide coupling and signal propagation, ensuring that the optical power delivered to each THz antenna remains close to **15 dBm**—the typical saturation power of the SOAs. The specific SOA integration strategy will be determined based on feedback from the experimental results of Precursor-1A and Demo-1A.

The entire system is designed to support operation up to **2 THz**. Both the OBFN and the CI stage will incorporate **heater-based phase shifters** capable of achieving full **2π phase modulation**.

2.5 Demo-1B: Multi-channel FMCW THz spectrometer with beamforming capabilities

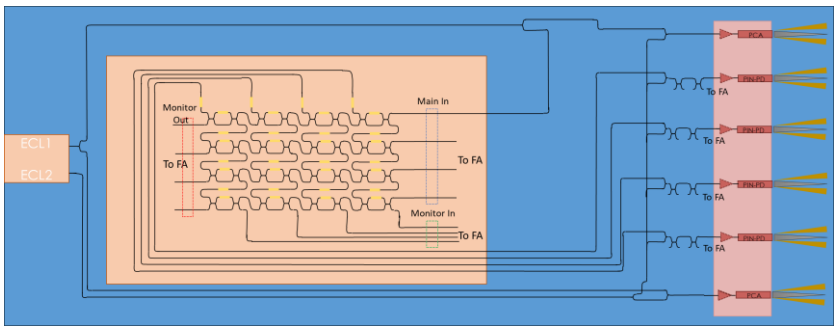

Figure 7. Functional design of Demo-1B.

Demo-1B represents the final and most advanced prototype in the FMCW THz spectrometer series within the POLYNICES project. Designed as the culmination of a structured, step-by-step development process, Demo-1B integrates and builds upon all the knowledge and architectural elements established in the earlier prototypes. For the first time, it will showcase a **fully integrated, multi-channel FMCW THz spectrometer**, highlighting the project's complete system capabilities. The functional layout of the prototype is illustrated in **Figure 7**.

The system architecture of Demo-1B is composed of **five key functional blocks**. The first of these is the **dual laser source module**, which mirrors the design successfully implemented in both **Precursor-0A and Demo-1A**. It features two **external cavity laser (ECL) sources**, each incorporating **two gain sections**, providing robust and tunable optical outputs. The design of the external cavities remains consistent with previous implementations, employing **thermo-optical phase shifters** to enable high-speed wavelength sweeping across the C-band—an essential requirement for FMCW-based THz generation.

The remaining three main components are adopted directly from **Precursor-1B**, ensuring continuity in system design and performance. These include the **4×4 optical beamforming network (OBFN)** based on the **Blass matrix architecture**, the **carrier insertion (CI) stage**, and the **THz antenna array**. All of these modules retain the same structure, configuration, and operating parameters as their counterparts in Precursor-1B.

By combining these components into a cohesive system, Demo-1B will not only validate the complete integration strategy of the POLYNICES platform but also demonstrate its readiness for scalable, high-resolution, and multi-directional THz spectroscopic applications.

2.6 Precursor-2A

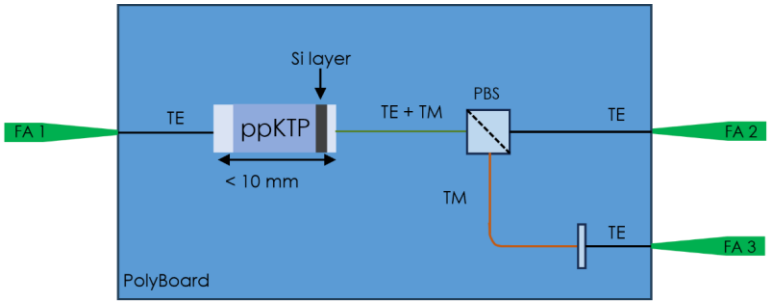

Figure 8. Functional design of Precursor-2A.

Figure 8 presents the functional design of **Precursor-2A**, the first prototype in the family of **quantum information processors** within the POLYNICES project. This prototype serves as a critical stepping stone toward the development of more advanced systems, particularly **Demo-2A**, by validating key integration steps and evaluating performance under realistic conditions.

The design is based on the **PolyBoard's micro-optical bench** [1]**.** At the input, a **standard single-mode fiber (SMF)** is aligned and coupled to the PolyBoard via **etched U-grooves**, ensuring precise and stable fiber placement. A **GRIN (graded-index) lens** is positioned immediately after the fiber to shape and focus the beam. This engineered beam then travels through a **free-space section**, where a **periodically poled potassium titanyl phosphate (ppKTP) crystal** is inserted. The crystal facilitates the nonlinear optical process—typically spontaneous parametric down-conversion (SPDC)—for generating entangled photon pairs.

Following the crystal, a second GRIN lens collects and re-shapes the optical beam for efficient coupling back into the on-chip **PolyBoard waveguide**. Once the light re-enters the guided platform, it encounters a **polarization beam splitter (PBS)**, which separates the **signal** and **idler** photons based on their polarization states. In the idler path, a **polarization rotator (PR)** is included to align its polarization with that of the signal, ensuring that both output channels have the same polarization state.

Both the PBS and PR are standard, well-established building blocks in the PolyBoard platform. They are realized using **thin-film elements**, precisely integrated into the waveguides through **etched slots**, offering compactness and stability.

At the output, the signal and idler photons are routed to **optical fibers**, which are also coupled to the PolyBoard using etched grooves, similar to the input. This approach ensures consistent alignment and minimal optical loss during coupling.

Precursor-2A will play a pivotal role in refining the fabrication process, validating component interoperability, and assessing system-level optical performance. Its results will directly inform the design and integration strategies of **Demo-2A**, helping to ensure the successful deployment of the full quantum information processing system.

2.7 Demo-2A

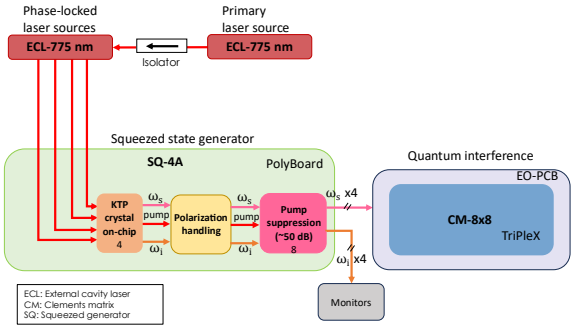

Figure 9. High-level building block design of Demo-2A.

Figure 9 presents the building block diagram of Demo-2A. The key building blocks of Demo-2A are the high-power laser source, array of KTP crystals, the on-chip optical filters and a Clements matrix. The system design for the prototype is primarily shaped by the characteristics of the KTP crystals. Market research for suitable KTP crystal suppliers, meeting specified criteria, revealed that the optical carrier's input to each KTP crystal should be <100 mW (<20 dBm). Considering the initial design of Demo-2A of having a single laser source, the ECL source output should be around 800 mW (29 dBm). However, a single ECL source cannot deliver such a high output power. Therefore, it is necessary to use multiple ECLs, each with two gain sections, coupled to individual ppKTP crystals, in order to meet the power requirements. However, increasing the number of integrated ECLs may lead to thermal instability, adversely affecting the performance of the crystals. To manage the thermal dissipation risks for the crystals, Demo-2A is split into three parts: the laser unit, the ppKTP unit and the quantum information processor all three interconnected via polarization maintained (PM) fibers.

Laser unit – The functional layout of the laser unit is depicted in Figure 10. Four dual-gain ECLs will generate high-power optical carriers. A fifth ECL will act as the master laser to phase-lock the four secondaries. The secondary ECLs will be paired on two TriPleX PICs; the primary will be integrated separately, its output isolated to prevent back-reflections before distribution to the PICs. The primary's optical carrier will be split on-chip and injected into the ECL cavities, then combined via a 2×2 coupler to adjust relative power levels before routing to the main submodule.

ppKTP crystal unit: Optical carriers at 775 nm will pump the ppKTP crystals to produce signal and idler photons at 1549 nm and 1551 nm. Polarization control in PolyBoard ensures TE polarization for both. Pump suppression exceeds 100 dB using silicon layers on the crystals and optimized directional couplers. The four signal photons will be further coupled to the third unit while the idle photons will be detected for monitoring purposes.

intended integration quantity. Consequently, 10 crystals are acquired, with plans to integrate 4 of them.

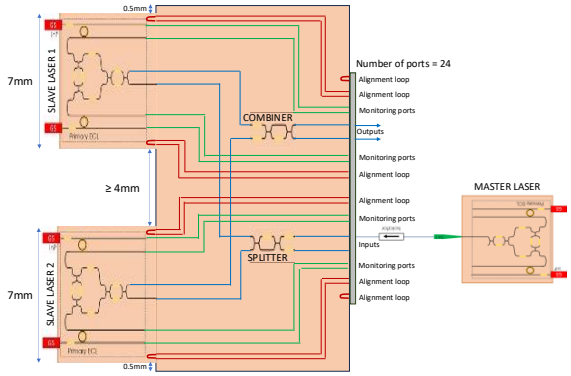

Figure 10. Functional design of the one of the two laser submodules of Demo-2A, consisting of three integrated ECLs. One ECL acts as primary (Master) and locks the phases of the optical carriers generated by the other two secondary (Slave) ECLs.

Quantum Processor unit – The functional layout of processor is illustrated in Figure 11. The unit consists of a TriPleX PIC implementing an 8×8 Clements matrix, flip-chip coupled to the EO-PCB. Four input photons are interfered within the matrix and routed via the fiber array to external single-photon photodiodes for detection.

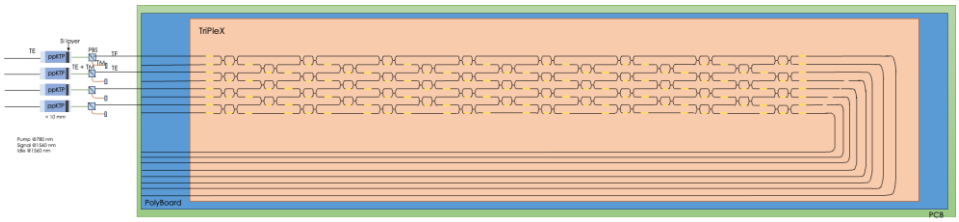

Figure 11. Functional design of the quantum information processor of Demo-2A.

2.8 Demo-2B

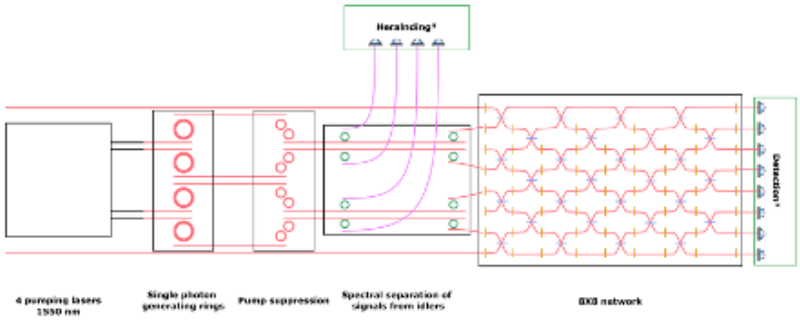

Figure 12. Functional design of Demo-2B.

Figure 12 presents the functional design of Demo-2B. The architecture of **Demo-2B** comprises of the following building blocks.

Photon-generating unit

The photon-generating unit of **Demo-2B** consists of four continuous-wave pumping lasers operating at a central wavelength of 1550 nm. These high-power optical carriers are coupled into an array of single-photon generating micro-ring resonators, specifically engineered to exploit the spontaneous four-wave mixing (SFWM) process for correlated photon-pair generation.

The main specification of the micro-ring resonators are reported in **Error! Reference source not found.**. More specifically, each micro-ring resonator is designed with the following specifications: a central wavelength of 1550 nm, a free spectral range (FSR) of 100 GHz, and an intrinsic quality factor $Q_{SFWM\_Intrinsic}$ exceeding 1×10^6. The resonators are over-coupled at 90–100 %, ensuring efficient extraction of the generated photons. The cavity dwelling time is set to $0.85 \cdot \Delta t$, where Δt — estimated between 100 ps and 1000 ps — is determined from the specific resonator geometry and fabrication tolerances. The output is taken from the Through port, enabling both generated frequency components to co-propagate along the same waveguide.

Under these conditions, each resonator produces a photon pair comprising a signal photon (~1551 nm) and an idler photon (~1549 nm), both sharing the same polarization state. This polarization uniformity removes the need for polarization handling components in later processing stages, simplifying integration and reducing optical loss.

Pump suppression stage

Residual pump light at 1550 nm is removed using pump filtering micro-ring resonators configured as a coupled resonator optical waveguide (CROW). Their specifications are summarized in **Error! Reference source not found.**. Light emerging at the Drop port of the CROW is directed to a beam dump to prevent pump leakage into subsequent stages.

Spectral separation of signal and idler photons

Following pump suppression, a spectral selection stage isolates the signal and idler channels using band-pass micro-ring resonators. The specification of this stage is reported in **Error! Reference source not found.**.

This separation enables idler photons to be routed to the heralding unit, where dedicated detectors record heralding events in real time. The signal photons are simultaneously directed into an 8 × 8 integrated interferometric network (Clements matrix) implemented in the TriPleX platform.

Quantum Processor unit

Within the Clements matrix, the signal photons undergo reconfigurable quantum interference. At the output, an array of off-PIC single-photon detectors measures the resulting states, enabling further quantum information processing.

3 FINAL SYSTEM SIMULATION STUDIES

3.1 Noise Analysis

In D2.2 a comprehensive analysis of the link gain regarding Demo-1A was presented. In this section we will examine the impact of noise introduced by the components of the setup, by calculating the power spectral density at each point for the various types of noise, as well as the signal-to-noise ratio at the receiver. For the purposes of this analysis, we assume detection of the optical signal by an ideal photodiode. Figure 14 represents a schematic diagram for Demo-1A, while Table 1, summarizes the system parameters which will be utilized in our calculations.

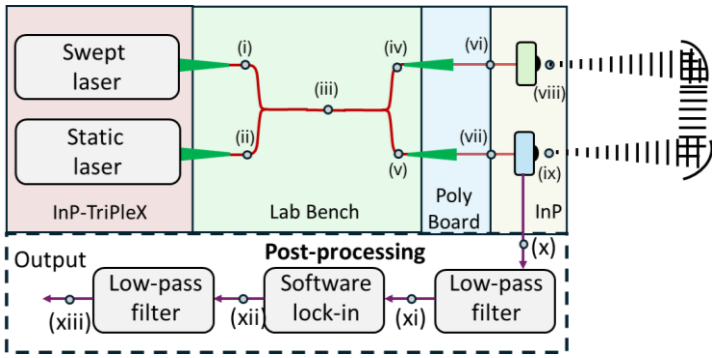

Figure 13. Schematic diagram of Demo-1A

Table 1 System parameters of the FMCW THz spectrometer simulation studies.

System Parameters			
Bandwidth (BW)	2 THz	$L_{TriPleX\text{-}FA}$	1.5 dB
Modulation frequency (f_{mod})	100 Hz	$L_{FA\text{-}Poly}$	1.5 dB
Modulation period (T_{mod})	10 ms	$L_{Poly\text{-}InP}$	3 dB
Power of swept laser ($P_{swept\ laser}$)	10 dBm	Polarization	TE
Power of static laser ($P_{static\ laser}$)	10 dBm	Starting frequency of swept laser (f_{start})	2 THz
Reflectivity (R_{sample})	-41.5	Refractive index (n_S)	2.42
Responsivity of photodiode (r_{pd})	0.3 A/W		

The three noise sources influencing the system performance are the following:

- Relative Intensity Noise of lasers (RIN)
- Shot Noise
- Thermal Noise

Before proceeding to the system noise analysis, a brief definition of each of the aforementioned phenomena is provided.

3.1.1 Relative Intensity Noise of lasers (RIN)

This type of noise describes fluctuations in the optical power of lasers and can undermine the stability and performance of the system. The sources of laser intensity noise may be either intrinsic or external. A primary cause is the spontaneous emission of electrons in the laser's active medium, which is a stochastic process. In addition, quantum mechanical phenomena—such as the statistical nature of photon behavior—can lead to fluctuations in the number of emitted photons, which directly affect the intensity of the emitted radiation. Another contributing factor is the specific facet of the laser from which photons are reflected and emitted. External conditions that can generate intensity noise include mechanical vibrations and disturbances in the system, temperature variations, and fluctuations in the pump current. Consequently, the actual amplitude of the optical signal is given by:

$$|E_s| = \sqrt{2 \cdot P_s + 2 \cdot \delta P(t)} \tag{1}$$

where $|E_s|$: is the amplitude of the optical field, P_s: the average optical power and $\delta P(t)$: the time-varying intensity fluctuations. We define the quantity RIN (Relative Intensity Noise) as the ratio of power variance to the square of the average optical power:

$$RIN = \frac{\langle P_{opt}^2(t) \rangle}{\langle P_{opt} \rangle^2} = \frac{\left\langle \left(P_{opt} - P_{opt,ave} \right)^2 \right\rangle}{P_{opt,ave}^2} \tag{2}$$

where the numerator represents the mean square value of the noise distribution, and the denominator corresponds to the average optical power. Since the electrical power after the photodiode is proportional to the square of the incident optical power (i.e. $P_{electrical} \propto P_{opt}^2$), the RIN quantity can be expressed as the ratio of the corresponding powers in the electrical domain, giving:

$$RIN = \frac{\langle P_{RIN,ML} \rangle}{P_{DC,ML}} \tag{3}$$

A typical RIN value is -165 dBc/Hz [2] where dBc refers to power normalized to the carrier's useful power. In order to study the lasers intensity noise in the electrical domain, especially for SNR calculation, we refer to the mean- squared current spectral density after the detection with photodiode.

3.1.2 Thermal Noise at Tx and Rx

Thermal noise is a consequence of fundamental principles of thermodynamics and statistical mechanics. Under conditions of thermal equilibrium, free electrons in a conductor acquire kinetic energy from heat, resulting in random "thermal" motion. This motion leads to random fluctuations in charge distribution and electric potential, which in turn causes voltage variations across the terminals of a resistor. The single-sided power spectral density of this noise is given by:

$$S_n(f) = 4 \cdot \frac{h \cdot f}{\exp\left(\frac{h \cdot f}{k_B \cdot T_s}\right) - 1} \tag{4}$$

where h: Planck's constant $\left(h = 6.625 \cdot 10^{-34} m^2 \cdot \frac{kg}{s}\right)$, T_s: the physical temperature and k_B: Boltzmann's constant $\left(k_B = 1.38 \cdot 10^{-38} \frac{m^2 \cdot kg}{s^2 \cdot K}\right)$. When the condition $h \cdot f \gg k_B \cdot T$ holds, the exponential term can be approximated using the Taylor series expansion:

$$\exp\left(\frac{h \cdot f}{k_B \cdot T_s}\right) = \sum_{n=0}^{\infty} \frac{1}{n!} \cdot \left(\frac{h \cdot f}{k_B \cdot T_s}\right)^n \approx 1 + \frac{h \cdot f}{k_B \cdot T_s} \tag{5}$$

Thus, thermal noise is considered to be white. The total thermal noise power generated across a resistor at temperature T_s over a bandwidth B is given by:

$$P_n = 4 \cdot k_B \cdot T_S \cdot B \tag{6}$$

A noisy resistor can be equivalently modeled by a current source in parallel with a noiseless resistance R_{th}. The single-sided power spectral density of the mean square current is derived as shown below:

$$\frac{P_n}{B} = \langle i_{th}^2 \rangle \cdot R_{th} \Rightarrow \langle i_{th}^2 \rangle = \frac{4 \cdot k_B \cdot T_s}{R_{th}} \tag{7}$$

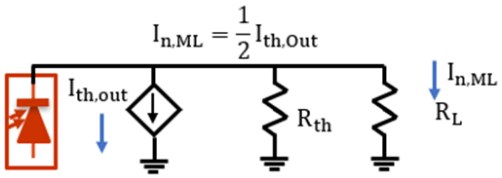

Figure 14. Equivalent output electrical circuit of photodiode at Tx-Thermal Noise.

The power spectral density of thermal noise across a resistor under impedance matching at the output of the photodiode is calculated with the help of Figure 15:

$$S_{th,ML} = \langle I_{th,ML}^2 \rangle \cdot R_L = \frac{1}{4} \cdot \langle i_{th}^2 \rangle \cdot R_L = k_B \cdot T_s \quad (8)$$

Thermal noise is generated directly in the electrical domain, in contrast to laser noise.

3.1.3 Shot Noise at Tx and Rx

In photodetectors, the average rate of detection events is constant. However, the actual number of photons absorbed and converted into electrons over a given time interval is random. Shot noise arises from this fluctuation and is associated with the particle nature of light. Statistically, it is modeled using Poisson distribution. The single-sided power spectral density of the variance of the corresponding current component, which is superimposed on the average photodiode current, is defined as follows:

$$\langle i_{shot}^2 \rangle = 2 \cdot q \cdot I_{dc} \quad (9)$$

Where q: is the fundamental electron's charge ($q = 1.6 \cdot 10^{-19}$ C) and I_{dc}: the average dc photocurrent. We observe that shot noise is proportional to the dc term of photocurrent an in turn of the incident optical power. According to Figure 16, the power spectral density of the shot noise across the matched load is given by:

$$S_{shot,ML} = \frac{1}{4} \cdot \langle i_{shot}^2 \rangle \cdot R_L = \frac{q \cdot I_{dc} \cdot R_L}{2} \quad (10)$$

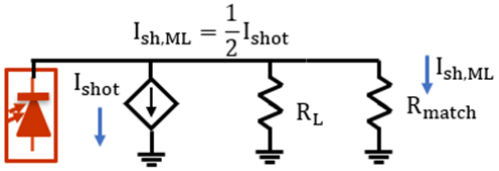

Figure 15. Equivalent output electrical circuit of photodiode at Tx-Shot Noise.

3.1.4 System Noise Analysis

Having provided the fundamental definitions of the various types of noise governing the system, we will proceed with the analysis of the noise components at each point of our setup, referring to Figure 14.

For the Relative Intensity Noise of lasers, we consider $RIN_{dB} = -165 \frac{dBc}{Hz}$, thus the power spectral density at their output will be equal to:

$$\rho_{ASE,rin} = P_c \cdot 10^{\frac{RIN_{dB}}{10}} = (3.162 \cdot 10^{-17}) \cdot P_c \quad (11)$$

where P_s: the power of the optical carrier. For both lasers the emitted optical power is equal to 10 dBm or 10 mW. So, from eq. (11) we obtain: $\rho_{ASE,rin} = (3.162 \cdot 10^{-16})$ mW.

Points (i) and (ii) after FA

The RIN power at points (i) and (ii) at the outputs of the corresponding fiber array ports, taking into account the interface losses between InP-TriPleX and FA, is equal to:

$$\rho_{1ASE,rin(i)} = \frac{P_{swept\ laser}}{L_{TriPleX\text{-}FA}} \cdot 10^{\frac{RIN_{dB}}{10}} \quad (12)$$

$$\rho_{2ASE,rin(ii)} = \frac{P_{static\ laser}}{L_{TriPleX\text{-}FA}} \cdot 10^{\frac{RIN_{dB}}{10}} \quad (13)$$

where index "1" stands for the swept laser and "2" for the static

Point (iii)

$$\rho_{1,ASE,rin(iii)} = \frac{1}{2} \cdot \frac{P_{swept\ laser}}{L_{TriPleX\text{-}FA}} \cdot 10^{\frac{RIN_{dB}}{10}} \quad (14)$$

$$\rho_{2,ASE,rin(iii)} = \frac{1}{2} \cdot \frac{P_{static\ laser}}{L_{TriPleX\text{-}FA}} \cdot 10^{\frac{RIN_{dB}}{10}} \quad (15)$$

$$\rho_{total,ASE,rin(iii)} = \rho_{1,ASE,rin(iii)} + \rho_{2,ASE,rin(iii)} = \frac{1}{2} \cdot \frac{P_{swept\ laser} + P_{static\ laser}}{L_{TriPleX\text{-}FA}} \cdot 10^{\frac{RIN_{dB}}{10}} \quad (16)$$

Points (iv) and (v)

$$\rho_{1,ASE,rin(iv),(v)} = \frac{1}{4 \cdot L_{TriPleX\text{-}FA}} \cdot P_{swept\ laser} \cdot 10^{\frac{RIN_{dB}}{10}} \quad (17)$$

$$\rho_{2,ASE,rin(iv),(v)} = \frac{1}{4 \cdot L_{TriPleX\text{-}FA}} \cdot P_{static\ laser} \cdot 10^{\frac{RIN_{dB}}{10}} \quad (18)$$

$$\rho_{total,ASE,rin(iv),(v)} = \rho_{1,ASE,rin(iv),(v)} + \rho_{2,ASE,rin(iv),(v)} = \frac{1}{4} \frac{P_{swept\ laser} + P_{static\ laser}}{L_{TriPleX\text{-}FA}} \cdot 10^{\frac{RIN_{dB}}{10}} \quad (19)$$

Points (vi) and (vii) at Polyboard

$$\rho_{1,ASE,rin(vi),(vii)-Poly} = \frac{1}{4 \cdot L_{TriPleX\text{-}FA} \cdot L_{FA\text{-}Poly}} \cdot P_{swept\ laser} \cdot 10^{\frac{RIN_{dB}}{10}} \quad (20)$$

$$\rho_{2,ASE,rin(vi),(vii)-Poly} = \frac{1}{4 \cdot L_{TriPleX\text{-}FA} \cdot L_{FA\text{-}Poly}} \cdot P_{static\ laser} \cdot 10^{\frac{RIN_{dB}}{10}} \quad (21)$$

$$\rho_{total,ASE,rin(vi),(vii)-Poly} = \rho_{1,ASE,rin(vi),(vii)-Poly} + \rho_{2,ASE,rin(vi),(vii)-Poly} =$$

$$\frac{1}{4}\frac{P_{\text{swept laser}} + P_{\text{static laser}}}{L_{\text{TriPleX-FA}} \cdot L_{\text{FA-Poly}}} \cdot 10^{\frac{RIN_{dB}}{10}} \quad (22)$$

Points (vi) and (vii) at InP

Considering that the interface loss between Polyboard and InP at PD and PCA respectively to be equal to each other, the same symbol "$L_{\text{Poly-InP}}$" is utilized in both cases.

$$\rho_{1,\text{ASE,rin(vi),(vii)}-\text{InP}} = \frac{1}{4 \cdot L_{\text{TriPleX-FA}} \cdot L_{\text{FA-Poly}} \cdot L_{\text{Poly-InP}}} \cdot P_{\text{swept laser}} \cdot 10^{\frac{RIN_{dB}}{10}} \quad (23)$$

$$\rho_{2,\text{ASE,rin(vi),(vii)}-\text{InP}} = \frac{1}{4 \cdot L_{\text{TriPleX-FA}} \cdot L_{\text{FA-Poly}} \cdot L_{\text{Poly-InP}}} \cdot P_{\text{static laser}} \cdot 10^{\frac{RIN_{dB}}{10}} \quad (24)$$

$$\rho_{\text{total,ASE,rin(vi),(vii)}-\text{InP}} = \rho_{1,\text{ASE,rin(vi),(vii)}-\text{InP}} + \rho_{2,\text{ASE,rin(vi),(vii)}-\text{InP}} = \frac{1}{4}\frac{P_{\text{swept laser}} + P_{\text{static laser}}}{L_{\text{TriPleX-FA}} \cdot L_{\text{FA-Poly}} \cdot L_{\text{Poly-InP}}} \cdot 10^{\frac{RIN_{dB}}{10}} \quad (25)$$

Assuming only RIN, the noise floor before the photodetection includes the RIN due to the swept laser and the RIN due to the static laser. Both noises reach the photodiode with the same power because we have defined:

$$P_{\text{swept laser}} = P_{\text{static laser}} = P_s \quad (26)$$

Consequently, at the input of PD we define:

$$\rho_{\text{ASE,rin}-\text{swept}-\text{PD}} = \frac{1}{4 \cdot L_{\text{TriPleX-FA}} \cdot L_{\text{FA-Poly}} \cdot L_{\text{Poly-InP}}} \cdot P_{\text{swept laser}} \cdot 10^{\frac{RIN_{dB}}{10}} \quad (27)$$

$$\rho_{\text{ASE,rin}-\text{static}-\text{PD}} = \frac{1}{4 \cdot L_{\text{TriPleX-FA}} \cdot L_{\text{FA-Poly}} \cdot L_{\text{Poly-InP}}} \cdot P_{\text{static laser}} \cdot 10^{\frac{RIN_{dB}}{10}} \quad (28)$$

The total link gain from the LS output to the PD or PCA input is defined as:

$$L_{Ls} = \left(\frac{1}{4 \cdot L_{\text{TriPleX-FA}} \cdot L_{\text{FA-Poly}} \cdot L_{\text{Poly-InP}}}\right)^{-1} \quad (29)$$

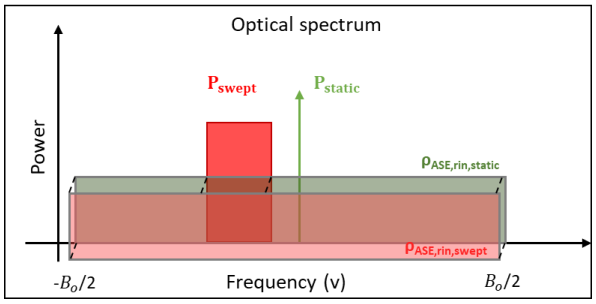

Figure 16. Optical Spectrum before photodetection assuming only RIN.

In the photodiode, beating will occur between the carrier of the swept laser and the noisy field of both the swept and the static laser, the carrier of the static laser with the noisy field of both lasers, as well as between the noise carriers of the two lasers themselves. The last term, however, is negligible. Also, for the laser noise, we consider the noise PSD at frequency offsets on both sides of the carriers, that is $f \pm \Delta f$. The optical spectrum before photodetection, consisting of the optical carrier accompanied by the respective RIN fields, is depicted in Figure 17.

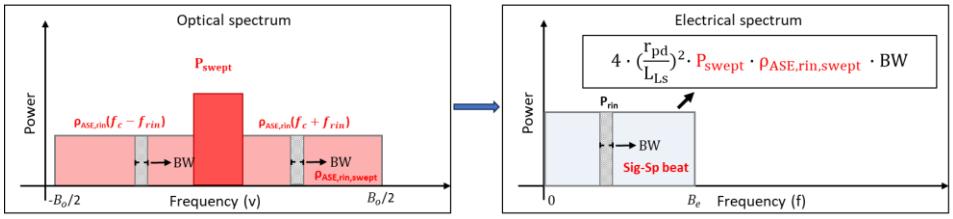

Figure 17. Beating between $P_{swept\ laser}$ and $\rho_{ASE,rin,swept}$.

Figure 18 provides a visual representation of the beating process between the carrier of the swept laser and the RIN field originating from the same carrier. The mathematical equation is given in the following:

$$I_{rin,\ swept\ LS,swept\ LS} = 2 \cdot r_{pd} \cdot \sqrt{\frac{P_{swept}}{L_{Ls}} \cdot \frac{\rho_{ASE,\ rin,swept}\ (f - \Delta f)}{L_{Ls}} \cdot B_e \cdot \cos(\theta_1(t))} + 2 \cdot r_{pd} \cdot \sqrt{\frac{P_{swept}}{L_{Ls}} \cdot \frac{\rho_{ASE,\ rin,swept}\ (f + \Delta f)}{L_{Ls}} \cdot B_e \cdot \cos(\theta_2(t))} \xrightarrow{\cos a + \cos b = 2 \cdot \cos\left(\frac{a-b}{2}\right) \cdot \cos\left(\frac{a+b}{2}\right)}$$

$$I_{rin,,\ swept\ LS,swept\ LS} = 2 \cdot r_{pd} \cdot \sqrt{\frac{P_{swept}}{L_{Ls}} \cdot \frac{\rho_{ASE,\ rin,swept}}{L_{Ls}} \cdot B_e \cdot 2 \cdot \cos\left(\frac{\theta_1(t) - \theta_2(t)}{2}\right) \cdot \cos\left(\frac{\theta_1(t) + \theta_2(t)}{2}\right)} \quad (30)$$

where $\theta_1(t)$, $\theta_2(t)$: the random phase difference between the nominal field and the noise field. The PSD of the corresponding noise component at the output of PD, equals the variance of the current, thus:

$$\langle I_{rin,\ swept\ LS,swept\ LS}{}^2 \rangle = \left(4 \cdot \frac{r_{pd}}{L_{Ls}} \cdot \sqrt{P_{swept} \cdot \rho_{ASE,\ rin,swept} \cdot B_e}\right)^2 \cdot \left\langle \cos\left(\frac{\theta_1(t) - \theta_2(t)}{2}\right)^2 \cdot \cos\left(\frac{\theta_1(t) + \theta_2(t)}{2}\right)^2 \right\rangle \xrightarrow{\langle \cos^2 \theta = \frac{1}{2} \rangle}$$

$$\langle I_{\text{rin, swept LS,swept LS}}{}^2 \rangle = 4 \cdot \left(\frac{r_{pd}}{L_{Ls}}\right)^2 \cdot P_{\text{swept}} \cdot \rho_{\text{ASE, rin,swept}} \cdot B_e \quad (31)$$

The noise PSD at matched load (R_L) is given as:

$$S_{\text{rin, swept LS,swept LS}} = \frac{1}{4} \cdot R_L \cdot \langle I_{\text{rin, swept LS,swept LS}}{}^2 \rangle = \frac{1}{4} \cdot R_L \cdot 4 \cdot \left(\frac{r_{pd}}{L_{Ls}}\right)^2 \cdot P_{\text{swept}} \cdot \rho_{\text{ASE, rin,swept}}$$
$$= R_L \cdot \left(\frac{r_{pd}}{L_{Ls}}\right)^2 \cdot N_{\text{swept}} \cdot \rho_{\text{ASE, rin,swept}} \Rightarrow N_{\text{rin, swept LS,swept LS}} = R_L \cdot \left(\frac{r_{pd}}{L_{Ls}}\right)^2 \cdot P_{\text{swept}} \cdot \rho_{\text{ASE, rin,swept}} \quad (32)$$

The power results from the respective PSD after multiplying with the electrical BW:

$$P_{\text{rin, swept LS,swept LS}} = R_L \cdot \left(\frac{r_{pd}}{L_{Ls}}\right)^2 \cdot P_{\text{swept}} \cdot \rho_{\text{ASE, rin,swept}} \cdot B_e \quad (33)$$

where B_e: the electrical bandwidth.

Following the same rationale, the following results for the remaining beating terms are derived:

$$S_{\text{rin, swept LS,static LS}} = R_L \cdot \left(\frac{r_{pd}}{L_{Ls}}\right)^2 \cdot P_{\text{swept}} \cdot \rho_{\text{ASE, rin,static}} \quad (34)$$

$$S_{\text{rin, static LS,swept LS}} = R_L \cdot \left(\frac{r_{pd}}{L_{Ls}}\right)^2 \cdot P_{\text{static}} \cdot \rho_{\text{ASE, rin,swept}} \quad (35)$$

$$S_{\text{rin, static LS,static LS}} = R_L \cdot \left(\frac{r_{pd}}{L_{Ls}}\right)^2 \cdot P_{\text{static}} \cdot \rho_{\text{ASE, rin,static}} \quad (36)$$

All four beating terms are uncorrelated to each other, so they do sum up. Taking into account eq. (26) the total RIN PSD after photodetection equals:

$$S_{\text{ML,RIN(Total)}} = R_L \cdot I_{dc}^2 \cdot 10^{\frac{\text{RIN}\left(\frac{\text{dBW}}{\text{Hz}}\right)}{10}} \quad (37)$$

where:

$$I_{dc} = \frac{r_{pd} \cdot P_s}{2 \cdot L_{\text{TriPleX-FA}} \cdot L_{\text{FA-Poly}} \cdot L_{\text{Poly-InP}}} \quad (38)$$

As has been described above, PSD of the thermal noise at the output of the photodetector at a matched load is given from the following expression:

$$S_{\text{thTx,ML}} = \frac{1}{4} \cdot \langle i_{th}^2 \rangle \cdot R_L = k_B T_s \quad (39)$$

Additionally, regarding the PSD of shot noise at the PD output across a matched resistance:

$$S_{\text{shotT}\chi\text{,ML}} = \frac{q \cdot I_{dc} \cdot R_L}{2} \quad (40)$$

where I_{dc} is calculated according to eq. (38)

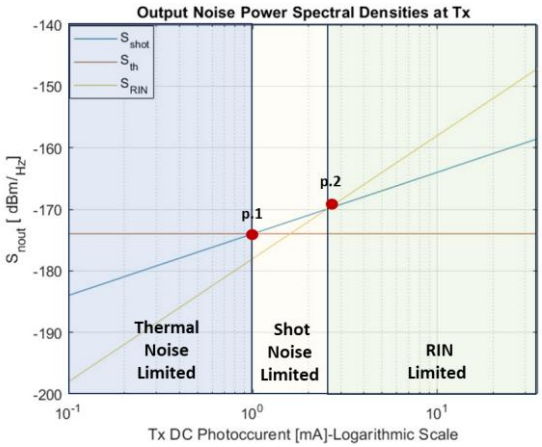

Figure 18. Noise PSDs at the Tx w.r.t Photocurrent

In Figure 19, the noise PSDs at the transmitter after photodetection are represented. Three distinct noise regions at the transmitter can be identified based on the value of the photodiode's DC current. Specifically, up to 0.98 mA, thermal noise dominates at the transmitter. For higher current values, shot noise becomes the limiting factor. This changes when the dc photocurrent reaches approximately 2.5 mA, at which point the dominant noise component is the laser intensity noise. For our operating parameters, the dc term equals 0.27 mA thus the systems lies at the first region. To mathematically demonstrate how the transition points between dominant noise components arise, we begin by noting that shot noise surpasses thermal noise when:

$$\frac{q}{2} \cdot I_{dc} \cdot R_L > k_B \cdot T_s \Rightarrow$$

$$I_{dc} > \frac{2 \cdot k_B \cdot T_s}{q \cdot R_L} = 0.98 \text{ mA} \quad (41)$$

Similarly, laser noise dominates over shot noise in the range where the following condition holds:

$$R_L \cdot RIN \cdot I_{dc}^2 > \frac{q}{2} \cdot I_{dc} \cdot R_L \Rightarrow$$

$$I_{dc} > \frac{q}{2 \cdot RIN} \approx 2.5 \text{ mA} \quad (42)$$

As we have seen, the emitted THz power is proportional to the square of the photodiode's DC current. Therefore, in the first region, given that thermal noise is independent of I_{dc}, the signal-to-noise ratio (SNR) at the transmitter is also proportional to the square of the current. As a result, increasing the current, by raising the laser power, is beneficial for improving performance. In the second region, the dependence of the SNR on I_{dc} becomes linear, as the dominant shot noise in this region is proportional to the current. Consequently, if the system operates in the second region, increasing the laser power will again enhance the transmitter's performance. However, compared to the first region, for a given increase in I_{dc}, the corresponding improvement in SNR will be halved in dB units. When the system becomes limited by RIN, the SNR becomes independent of the current. Therefore, it is evident that increasing the current beyond 2.5 mA is not desirable, as it results in higher power consumption without any further improvement in SNR. These conclusions are also illustrated in Figure 20.

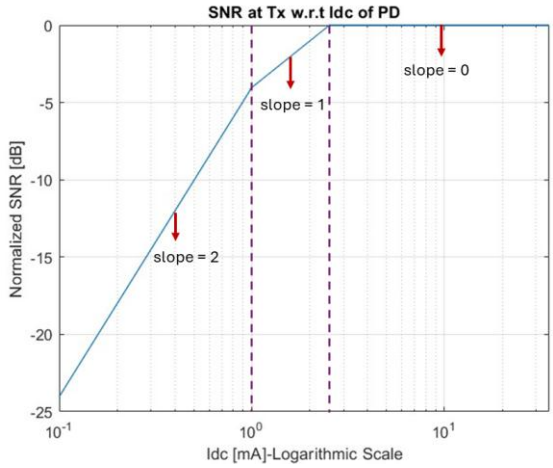

Figure 19. SNR at the Tx w.r.t the dc photocurrent

Briefly, we have the following relationships:

$$\mathrm{SNR_{Tx}} = \frac{\mathrm{P_{THz,DRW}}}{\mathrm{P_{noise}}} \text{ where } \mathrm{P_{THz,DRW}} = \frac{1}{8} \cdot \mathrm{I_{dc}^2} \cdot \mathrm{R_L} \tag{43}$$

Region 1

$$\mathrm{SNR_{Tx}} \propto \frac{\mathrm{I_{dc}^2}}{\mathrm{const}} \sim \mathrm{I_{dc}^2}\ \acute{\eta}\ 2 \cdot \mathrm{I_{dc}}\ \sigma\varepsilon\ \mathrm{dB} \tag{44}$$

Region 2

$$\mathrm{SNR_{Tx}} \propto \frac{\mathrm{I_{dc}^2}}{\mathrm{I_{dc}}} \sim \mathrm{I_{dc}}\ \acute{\eta}\ \mathrm{I_{dc}}\ \sigma\varepsilon\ \mathrm{dB} \tag{45}$$

Region 3

$$\mathrm{SNR_{Tx}} \propto \frac{\mathrm{I_{dc}^2}}{\mathrm{I_{dc}^2}} \sim \mathrm{I_{dc}}\ \acute{\eta}\ 0\ \mathrm{dB} \tag{46}$$

After the transmitter, the noise, similarly to the signal, is subject to free-space losses according to Friis' law:

$$\mathrm{g_{THz}} = \left(\frac{\mathrm{c}}{4 \cdot \pi \cdot \mathrm{L_{thz}}}\right)^2 \frac{1}{\mathrm{f^2}} \tag{47}$$

As a result, the power spectral densities of the noise components become frequency-dependent, and thus, the noise arriving at the receiver is no longer white. Additionally, the receiver antenna collects environmental noise, which is modeled as thermal noise with available power at its terminals given by:

$$\mathrm{N_k} = \mathrm{k_B} \cdot \mathrm{T_k} \cdot \mathrm{B} \tag{48}$$

where $\mathrm{k_B}$: Boltzmann's constant, B: the operational bandwidth and $\mathrm{T_k}$: the equivalent antenna noise temperature. The latter depends on various factors, such as the antenna's directional characteristics and orientation, the operating frequency, the climatic conditions of the installation site, and the time of year. However, since the application under study will be deployed indoors, room temperature is

assumed with $T_k = 290\ °K$. Therefore, for the power spectral densities of the noise at the receiver input, we have:

$$S_{th,Rx} = k_B \cdot T \cdot G_{Tx} \cdot G_{Rx} \cdot \left(\frac{c}{4 \cdot \pi \cdot L_{thz}}\right)^2 \cdot \frac{1}{f^2} \quad (49)$$

$$S_{shot,Rx} = \frac{q \cdot I_{dc} \cdot R_L}{2} \cdot G_{Tx} \cdot G_{Rx} \cdot \left(\frac{c}{4 \cdot \pi \cdot L_{thz}}\right)^2 \cdot \frac{1}{f^2} \quad (50)$$

$$S_{RIN,Rx} = R_L \cdot RIN \cdot I_{dc}^2 \cdot G_{Tx} \cdot G_{Rx} \cdot \left(\frac{c}{4 \cdot \pi \cdot L_{thz}}\right)^2 \cdot \frac{1}{f^2} \quad (51)$$

$$S_k = k_B \cdot T_k \quad (52)$$

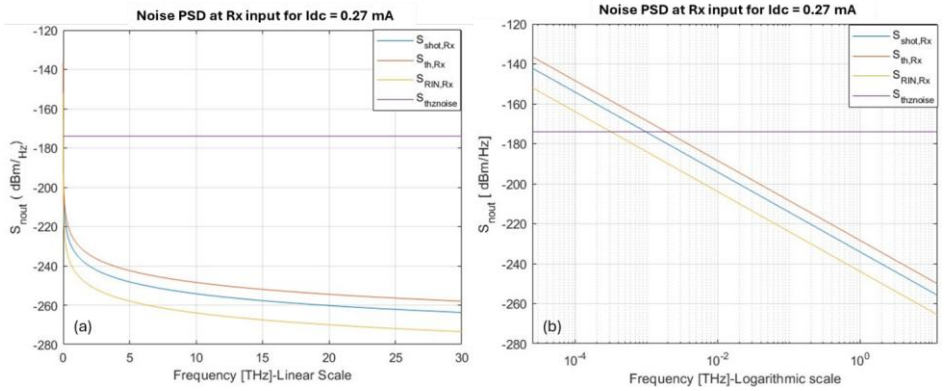

Figure 20. (a) PSD of noise components at receiver input after propagation at free space in linear scale and (b) PSD of noise components at receiver input after propagation at free space in logarithmic scale

In Figure 20. (a) we illustrate the power spectral densities of the noise components reaching the receiver after Friis attenuation and antenna gain, for the specific current value of our setup, $I_{dc} = 0.27\ mA$. As observed, apart from the ambient noise collected by the antenna, the noise power spectral densities exhibit a $1/f^2$ dependence. In Figure 20. (b), the same power spectral densities are shown on a logarithmic scale, in order to reveal their behavior at lower frequencies. On a logarithmic scale, the $1/f^2$ behavior appears as a slope of -2 with respect to frequency. It is evident that, from approximately 2 GHz onwards, the dominant noise source is the ambient noise collected by the antenna, as the remaining components have been significantly attenuated.

In addition to Friis attenuation, the noise also propagates through the sample and undergoes multiple reflections, just like the "useful" signal. We can consider only the first three reflected noise components, as the ones with considerable power will have been significantly attenuated. According to the Fabry–Perot equations, the first reflected component experiences additional power attenuation by a factor of R_{sample}, the second by $(1 - R_{sample}) \cdot R_{sample}$, and the third by $(1 - R_{sample}) \cdot R_{sample} \cdot R_{sample}^2$ where R_{sample} is the refractive index given in Table 1.

Noise is also introduced at the receiver from the lower optical path of the 3 dB splitter. As has been explained in D 2.2, the photoconductive element is illuminated with optical power equal to

$$P_{LO} = \frac{E_{LO} \cdot E_{LO}^*}{2} \quad (53)$$

and therefore, we observe a mathematically equivalent operation to that of the photodiode at the transmitter (Tx). The DC component of the generated power is equal to:

$$P_{LO,DC} = \frac{P_{\text{swept laser}} + P_{\text{static laser}}}{4 \cdot L_{\text{TriPleX-FA}} \cdot L_{\text{FA-Poly}} \cdot L_{\text{Poly-InP}}} \quad (54)$$

Taking into account the conversion losses, we can define an expression analogous to the photodiode's DC current:

$$I_{LO} = \frac{P_{LO,DC}}{L_{PCA}} = \frac{I_{dc}}{L_{PCA} \cdot r_{pd}} \quad (55)$$

where I_{dc}: is the DC current of the photodiode at the transmitter, and L_{PCA}: represents the conversion losses in the photoconductive antenna element (PCA) at the receiver (see Table 1), which include the necessary factor for impedance matching. Therefore, we can derive the expressions for the power spectral densities at the receiver from the corresponding expressions for the transmitter (Tx) noise components, by multiplying I_{dc}: by the factor "$\frac{1}{L_{PCA} \cdot r_{pd}}$".

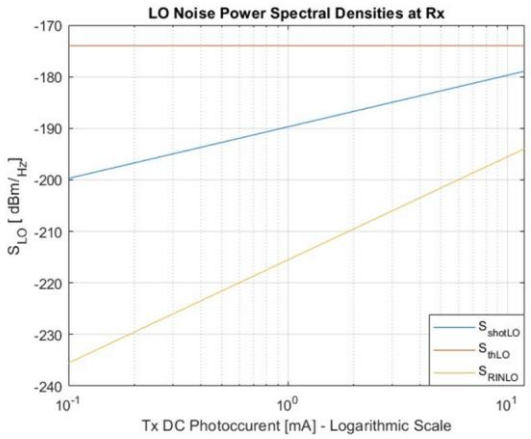

Figure 21. PSDs of noise components at the Local Oscillator (LO) side of the PCA

Thus, the single-sided power spectral densities of the noise components across the local oscillator load R_{LO} accounting for conversion losses, are as follow:

$$S_{th,LO} = 4 \cdot k \cdot T \quad (56)$$

$$S_{shot,LO} = 2 \cdot q \cdot I_{dc} \cdot R_{LO} \cdot \left(\frac{1}{L_{PCA} \cdot r_{pd}}\right) \quad (57)$$

$$S_{RIN,LO} = 4 \cdot R_{LO} \cdot RIN \cdot I_{dc}^2 \cdot \left(\frac{1}{L_{PCA} \cdot r_{pd}}\right)^2 \quad (58)$$

Next, we present a diagram of the equivalent circuit of the receiver, where Z_{LO} denotes the impedance of the local oscillator, Z_k the input impedance of the antenna, and Z_{IF} the output impedance receiving the intermediate frequency (IF) signal. Conjugate matching is assumed between Z_{LO} and Z_{IF}, as well as between Z_k and the parallel combination of the former two. That is:

$$Z_{LO} = Z_{IF} \quad (59)$$

and

$$Z_k = Z_{LO} \parallel Z_{IF} = \frac{Z_{LO}}{2} \quad (60)$$

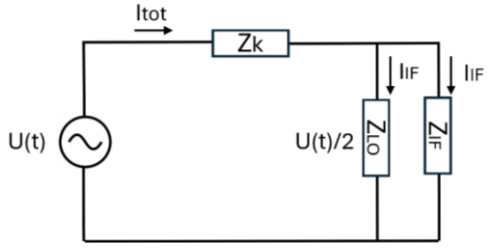

Figure 22. Input equivalent electrical circuit of receiver

Then, for the total IF current as well as for the portion that ultimately flows through the load, we have:

$$I_{tot} = \frac{U(t)}{Z_k + Z_{LO} \,//\, Z_{IF}} = \frac{U(t)}{Z_{LO}} \tag{61}$$

$$I_{IF} = \frac{I_{tot}}{2} \tag{62}$$

Equation (62) results from dividing the total current I_{tot} between the equal resistances Z_{LO} and Z_{IF}. Based on the above, the intermediate frequency (IF) current through the load is calculated as follows:

$$I_{IF} = \frac{1}{2} \cdot \left(\frac{P_{LO}}{L_{PCA}} \cdot U(t) \right) = \frac{1}{2} \cdot G_{LO} \cdot U(t) \tag{63}$$

With U(t) denoting the THz signal incident on the receiver antenna. That is, the current results from the multiplication of the two individual signals arriving at the PCA.

The received noise power across the load $Z_{IF} = R_{IF}$ (assuming resistive behavior) is given by:

$$S_{IF,noise} = I_{IF,noise}^2 \cdot R_{IF} = \frac{I_{tot,noise}^2}{4} \cdot R_{IF} = \frac{S_{tot,noise}}{4} \tag{64}$$

where analogous expressions to (61) through (63) apply for the noisy current components.

The total signal at the input of the receiver antenna will consist of the "useful" THz signal and the noise components originating from the transmitter after attenuation. On the side of the local photonic oscillator, we will have the photoconductive response G(t) along with the white noise components of the local oscillator. The multiplication of G(t) with the THz signal yields the "useful" IF signal, which we have already analyzed in D 2.2. The total noise will result from the following combinations:

- The multiplication of the THz signal with the white noise from the local oscillator
- The multiplication of the G(t) signal with the attenuated noise at the antenna input
- The interaction between the two "groups" of noise components themselves

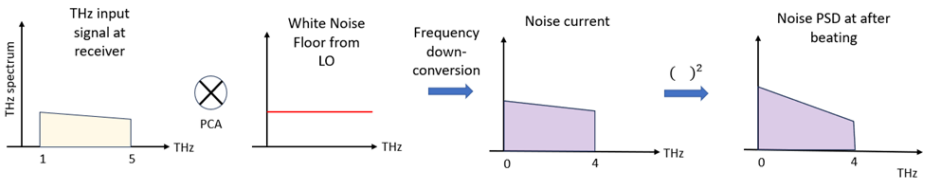

Figure 23. Multiplication of the THz useful signal with white noise from local oscilator (LO)

In order to multiply the appropriate terms, we must take the square root of the power spectral density from the local oscillator divided by the load resistance R_L so as to obtain a signal dimensionally equivalent to the photoconductivity G(t): $S_{LO,tot} \rightarrow \sqrt{\frac{S_{LO,tot}}{R_L}}$. The resulting signal after multiplication has the dimensions of current, consistent with the IF current it accompanies. The corresponding noise power spectral density is equal to the square of this noise current. Following the multiplication, as illustrated in Figure 24, the spectral content of the signal is shifted downward in frequency. This shift arises from the identity: $\cos(\varphi_1(t)) + \cos(\varphi_2(t)) = \frac{1}{2} \cdot [\cos(\varphi_1(t) + \varphi_2(t)) + \cos(\varphi_1(t) - \varphi_2(t))]$, where $\varphi_1(t)$ and $\varphi_2(t)$ are the phases of the signal and the noise, respectively. Naturally, power will also be present at higher frequencies, but we are primarily interested in the content up to several hundred kilohertz, since the noise power will be derived from the integration of the power spectral density over the bandwidth of the receiver's low-pass filter: $B_{LP} = 1.2 \cdot f_{IFref} = 640\ \text{kHz}$.. It should be noted that a factor of "1/4" must also be applied to account for the conjugate termination at the receiver, with $R_{IF} = R_L$.

For the noise at the input of the receiver antenna, it should be noted that the antenna will reject very low frequencies, just as in the case of the transmitter. At the receiver, we assume that $f_{cut,ant}$ is on the order of several hundred GHz. Therefore, the multiplication of the DC component of the photoconductivity G(t) with the noise from the transmitter and the ambient noise at the receiver input will yield spectral content outside the frequency band of interest. Regarding the frequency f_{env}, above which ambient noise becomes dominant, it is approximately equal to 2 GHz. Similarly, the multiplication of the AC component of the photoconductivity with the transmitter noise will result in spectral content that is filtered out by the low-pass filter. Consequently, we consider that the second component of the noise current arises from the following multiplication: $G_{AC}(t) \cdot \sqrt{\frac{S_{THz}}{R_L}}$, where $G_{AC}(t)$ is the AC term of photoconductance. We take the square root of the ambient noise power spectral density divided by the load resistance so that the resulting quantity has the same field units as the useful signal $E_{THz,Rx}$ at the receiver input. This is then squared and integrated over the bandwidth B_{LP} to obtain the noise power resulting from the second multiplication. The factor "1/4" is again included to account for the conjugate termination at the receiver. Figure 25. (a) illustrates schematically the antenna filtering of the input noise at receiver while Figure 25. (b) represents the multiplication of the respective noise components.

Regarding the third multiplication, visually described in Figure 26, both the noise from the local oscillator (LO) and the noise at the input of the receiver antenna occupy a wide spectral range. As a result, the outcome of their interaction will lie within the bandwidth of the low-pass filter.

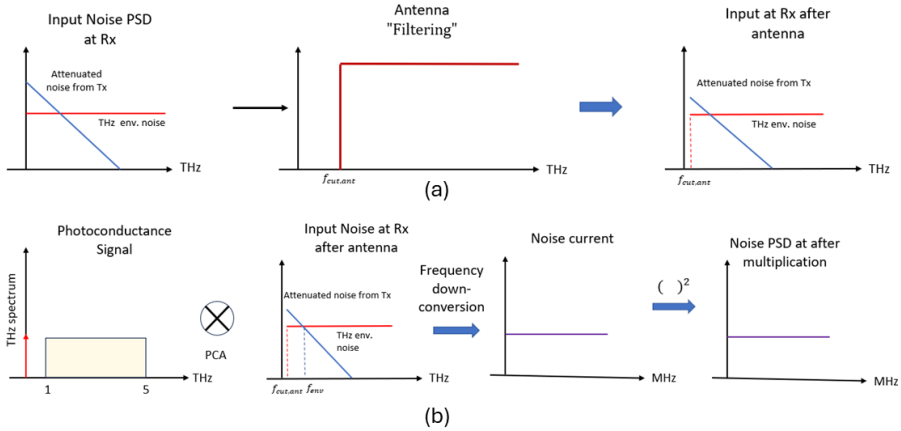

Figure 24. (a) Antenna filtering of input noise at receiver and (b) Multiplication of the photoconductance signal with the input noise at receiver.

The appropriate form of the terms being multiplied is: $\sqrt{\frac{S_{LO,tot}}{R_L}}$ and $\sqrt{\frac{S_{Rx,tot}}{R_L}}$ respectively. Explicitly, it holds that:

$$I_{IF,noise3} = \frac{1}{2} \cdot \sqrt{\frac{\left(S_{SOA,Rx} + S_{shot,Rx} + S_{RIN,Rx} + S_{th,Rx} + S_{THz}\right)}{R_L} \cdot \frac{\left(S_{SOA,LO} + S_{shot,LO} + S_{RIN,LO} + S_{th,LO}\right)}{R_L}} \quad (65)$$

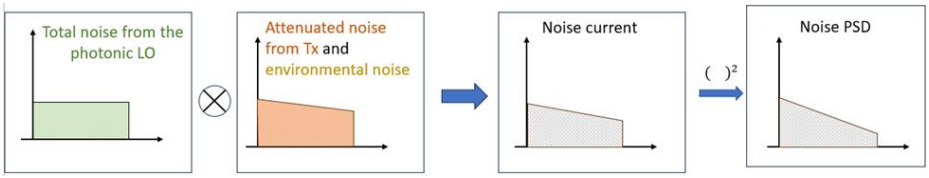

Figure 25. Multiplication of noise originating from the local oscillator (LO) side with noise at the input of antenna at receiver, including attenuated noise from transmitter and environmental noise

However, apart from the pair $(S_{RIN,Rx}, S_{RIN,LO})$ all other noise components are uncorrelated, as they arise from stochastic processes that evolve according to a probability distribution, in this case, the Gaussian distribution. If two variables following a Gaussian distribution are uncorrelated, then they are also independent. Let noise1 and noise2 be two uncorrelated noise variables. Then, the following holds:

$$S_{noise1} \cdot S_{noise2} = \langle i^2_{noise1} \rangle \cdot \langle i^2_{noise2} \rangle \xrightarrow{i^2_{noise1} \perp\!\!\!\perp i^2_{noise2}}$$

$$S_{noise1} \cdot S_{noise2} = \langle i^2_{noise1} \cdot i^2_{noise2} \rangle = R_{i^2_{noise1}, i^2_{noise2}}(t_1, t_2) \xrightarrow{\text{uncorrelated}}$$

$$S_{noise1} \cdot S_{noise2} = 0 \quad (66)$$

where R(,) is the auto-correlation function.

The noise fields originating from the lasers are correlated, as it stems from the same source with a slight delay, shorter than the coherence time. As a result, the noise power spectral density at the receiver is ultimately given by the following expression:

$$I_{IF,noise3} = \frac{1}{2} \cdot \sqrt{\frac{\left(S_{SOA,Rx} \cdot S_{SOA,LO} + S_{RIN,Rx} \cdot S_{RIN,LO}\right)}{R_L}} \tag{67}$$

The factor "1/2" corresponds to the portion of the current that reaches the load R_{IF} under conjugate matching conditions, and for power calculations, it becomes "1/4", as previously discussed. Now, taking into account the internal reflections within the sample, for the first three reflected components, the total power spectral density is given by:

$$S_{IFnoise,tot} = R_{sample} \cdot S_{IF} + R_{sample} \cdot \left(1 - R_{sample}\right)^2 \cdot S_{IF} + R_{sample}^2 \cdot R_{sample} \cdot \left(1 - R_{sample}\right)^2 \cdot S_{IF} \tag{68}$$

An exception is the term arising from the second multiplication since the ambient noise is not related to propagation phenomena within the sample. As previously mentioned, the total noise is obtained by integrating $S_{IF,noise}$ over the appropriate bandwidth. Specifically, as stated earlier, we assume the use of a low-pass filter with a cutoff frequency 20% higher than f_{IFref}:

$$B_{LP} = 1.2 \cdot f_{IFref} = 640 \text{ kHz} \tag{69}$$

Then, the noise power across the load $R_L = R_{IF}$ will be given from the following expression:

$$P_{IF,noise} = R_L \cdot \int_0^{B_{LP}} S_{IFnoise,tot} \, df \tag{70}$$

Regarding the power of the IF signal:

$$P_{IF} = \langle I_{IF}^2 \rangle \tag{71}$$

While the power across the resistance R_{IF}, considering $R_{IF} = 50\ \Omega$ equals:

$$P_{IF,R_{IF}} = \langle I_{IF}^2 \rangle \cdot R_{IF} \tag{72}$$

Utilizing Equations (70) and (72), we calculate the signal-to-noise ratio at the system output:

$$SNR_{out} = \frac{P_{IF,R_{IF}}}{P_{IF,noise}} = 21.14 \text{ dB} \tag{73}$$

Above, a comprehensive computational approach for the noise power at the system output was outlined. However, it is interesting to note that the dominant noise component at receiver, is that arising from the multiplication of the antenna's thermal noise with the photoconductance G(t), because it is the only one that is not affected by Friis attenuation. This observation can be also inferred from Figure 27, where the total noise power as well as the noise power of the dominant component w.r.t RIN of lasers is plotted. As seen, for the whole investigated range of RIN values, the total noise power coincides with the power of the dominant noise component, meaning that the other terms are negligible.

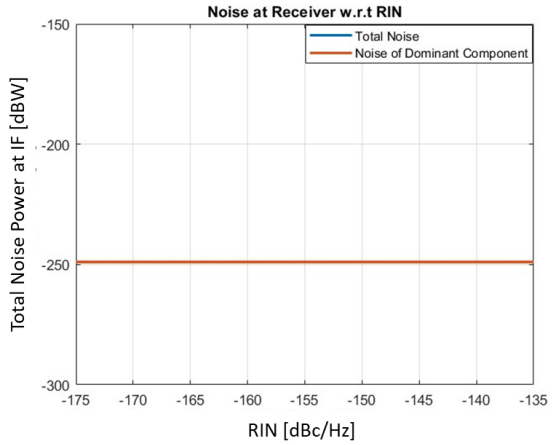

Figure 26. Dominant noise component at receiver as well as total noise power w.r.t RIN of lasers

If we take into account only the dominant noise component, then the PSD of the total noise at the Rx output can be expressed as:

$$S_{noise} = S_{noise3} = \frac{1}{32} \cdot \left(G_{AC}(t) \cdot \sqrt{\frac{S_{Th,Ant}}{R_L}} \right)^2 \cdot R_L = \frac{1}{32} \cdot \frac{1}{4} \cdot \frac{P_s^2 \cdot k \cdot T_k}{L_{PCA}^2} \quad (74)$$

The power of the IF signal w.r.t the optical power is equal to:

$$P_{IF} = \frac{1}{2} \cdot \frac{1}{32} \cdot \frac{r_{pd}^2 \cdot P_s^4 \cdot R_{sample} \cdot \overline{g_{THz}} \cdot R_L}{L_{PCA}^2} \quad (75)$$

where $\overline{g_{THz}}$ is the average value of Fris attenuation. Then the SNR at receiver can be expressed as:

$$SNR_{Rx} = \frac{P_{IF}}{S_{noise}} \sim \frac{r_{pd}^2 \cdot P_s^2 \cdot R_{sample} \cdot \overline{g_{THz}} \cdot R_L}{k \cdot T_k} \quad (76)$$

As can be concluded from equation (76), the SNR at receiver is proportional to the square of the optical power. The corresponding graph is given in Figure 28.

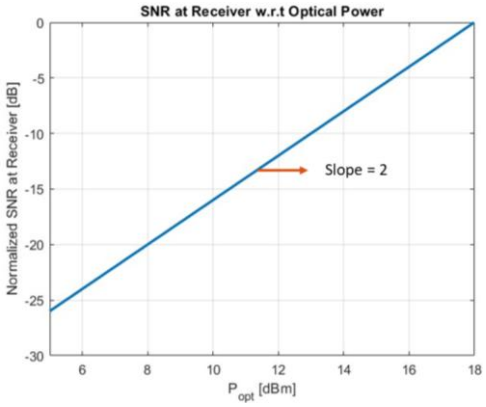

Figure 27. SNR at receiver w.r.t the optical power

3.1.5 Laser Phase Noise

The ideal carrier at the output of a laser is an optical wave with constant amplitude, frequency, and phase. In practice, however, this is impossible to achieve completely. Spontaneously emitted photons induce fluctuations in the amplitude and phase of the carrier, which are described as noise. Thus, the actual carrier of a continuous-wave laser can be expressed in the form:

$$\overrightarrow{E_{cw}(t)} = \sqrt{2 \cdot P_s + 2 \cdot \delta P(t)} \cdot \exp\left[j\left(\omega_s t + \varphi_s + \varphi_{ns}(t)\right)\right] \cdot \hat{e}_s \quad (77)$$

where ω_s: the optical frequency, φ_s: the initial phase and $\varphi_{ns}(t)$: the laser phase noise.

The intensity noise of the laser has already been examined in previous sections. In this section, we will focus on phase noise. In the general case, the phase information is lost after the detection of a signal by a photodiode. However, in our architecture, the input signal consists of the superposition of two carriers, and the resulting photocurrent includes both a constant term and a sinusoidal term that contains the phase difference between the two individual carriers. Consequently, the phase noise propagates within the signal and must be taken into account. Phase noise, therefore, originates from the spontaneous emission of photons with random phase relative to the photons of stimulated emission. The evolution of the total phase over time can be considered as a sequence of random steps, following a probability distribution in a mathematical space. Within a time interval τ, the phase undergoes a random shift given by:

$$\Delta_{\varphi_{ns}}(\tau) = \varphi_{ns}(t) - \varphi_{ns}(t-\tau) \quad (78)$$

The random phase shifts $\Delta_{\varphi_{ns}}(\tau)$ result from a large number of independent stimulated emission events. Therefore, according to the Central Limit Theorem, they can be modeled as samples from a Gaussian distribution. Furthermore, by making the realistic assumption that the frequency noise $\dot{\varphi}_{ns}(t)$ is white with power spectral density $W_{\dot{\varphi}_{ns}}(t) = \frac{2}{t_c}$ the variance of the phase noise is given by:

$$\left\langle \Delta^2_{\varphi_{ns}}(\tau) \right\rangle = W_{\dot{\varphi}_{ns}}(t) \cdot |\tau| = \frac{2 \cdot |\tau|}{t_c} \quad (79)$$

where t_c: the laser's coherence time. The physical meaning of the coherence time is that two optical waves emitted by the same laser with a time difference $\Delta\tau$ remain correlated when they interfere, provided that the condition $\Delta\tau < t_c$ is satisfied.

Taking phase noise into account, the optical field of a static laser is, in reality, composed of a sum of frequencies that define its bandwidth. Thus, the interference of two temporally delayed optical fields originating from the same source results from the superposition of the interference of their individual frequency components, since optical waves of different frequencies are considered mutually uncorrelated. Instead of the ideal Dirac function, the power spectral density of a real laser's optical field can be described by the Lorentzian distribution:

$$W_E(\omega) = \frac{2 \cdot t_c \cdot P_s}{1 + [(\omega - \omega_s) \cdot t_c]^2} \quad (80)$$

The laser linewidth is defined as the half-power bandwidth. If ω_r is the frequency at which the amplitude of the power spectral density equals half of its maximum value, to the right of ω_s, then from equation (80) we have:

$$\frac{2 \cdot t_c \cdot P_s}{1 + [(\omega_r - \omega_s) \cdot t_c]^2} = t_c \cdot P_s \Rightarrow$$

$$[(\omega_r - \omega_s) \cdot t_c]^2 = 1 \Rightarrow$$

$$\Delta\omega_r = \frac{1}{\tau c} \quad (81)$$

The same relation also holds for the frequency ω_l to the left. Therefore, the total angular linewidth is equal to:

$$\omega_s = \frac{2}{\tau c} \tag{82}$$

and in terms of frequency:

$$\Delta v_s = \frac{\Delta\omega_s}{2\pi} = \frac{1}{\pi t_c} \tag{83}$$

We observe that the laser linewidth and the coherence time are inversely proportional quantities. The narrower the linewidth, the greater the coherence time, and consequently, the higher the correlation factor between optical fields with a relative time delay. In the ideal case where the laser is represented by a Dirac delta function in the frequency domain, the coherence time is infinite. By substituting equation (83) into equation (79), the variance of the phase shift can be expressed as follows:

$$\left\langle \Delta^2_{\varphi_{ns}}(\tau) \right\rangle = 2 \cdot \pi \cdot \Delta v_s \cdot \tau \tag{84}$$

The above expression shows that phase uncertainty increases with the laser linewidth, which is consistent with the previous observations as well as with the observation time.

Let $\varphi_{ns,\text{swept laser}}(t)$ represent the phase noise of the modulated (swept) laser, and $\varphi_{ns,\text{static laser}}(t)$ represent the phase noise of the static laser. Since these variables are statistically independent, the total noise resulting from the superposition of the two optical fields will also follow a normal distribution, with a variance equal to the sum of the individual variances:

$$\varphi_{ns,total}(t) = \varphi_{ns,\text{swept laser}}(t) - \varphi_{ns,\text{static laser}}(t) \tag{85}$$

$$\sigma^2_{\varphi_{ns,total}} = \sigma^2_{\varphi_{ns,\text{swept laser}}} + \sigma^2_{\varphi_{ns,\text{static laser}}} \tag{86}$$

Thus, the total phase of the IF signal, including noise, is given by:

$$\varphi_{IF}(t) = \varphi_{FMCW}(t - \tau_{THZ}) - \varphi_2(t - \tau_{THz}) - \varphi_{FMCW}(t) + \varphi_2(t) + \pi =$$

$$2\pi \cdot \left((\text{slope} \cdot \tau_{THz})t + f_0 \cdot \tau_{THz} - \frac{1}{2} s \cdot \tau^2_{THz} \right) + \pi + \varphi_{ns,total}(t - \tau_{THz}) - \varphi_{ns,total}(t) \Rightarrow$$

$$\varphi_{IF}(t) = 2\pi \cdot f_{IF} \cdot t + 2\pi \cdot \left(f_0 \cdot \tau_{THz} - \frac{1}{2} s \cdot \tau^2_{THz} \right) + \pi + \delta_{\varphi_{ns}}(\tau_{THz}) \tag{87}$$

As seen from the above expression, the phase noise of the lasers induces phase noise in the final intermediate frequency (IF) signal as well.

In Figure 29. (a)-(d) we illustrate the superimposed optical spectrum after the 3 dB coupler, consisting of the static and swept carrier for the ideal case, for $\Delta_{vs} = 10$ kHz, for $\Delta_{vs} = 100$ kHz and for $\Delta_{vs} = 5$ MHz respectively. As expected, for larger bandwidths, the deviation from the ideal shape becomes more pronounced. However, the noise corresponding to linewidths from 50 Hz to 5 MHz, as observed, did not significantly affect the positions or amplitudes of the peaks in the Fourier transform of the intermediate frequency signal. Therefore, the phase noise of the lasers is not a limiting factor for the measurement accuracy. At the theoretical level, in order to avoid distortion, the relative delay of the signals at the receiver must be smaller than the coherence time of the lasers, that is:

$$t_{THz} < t_c \tag{88}$$

where $t_{THZ} = 1.33$ ns. The coherence times corresponding to the laser linewidths are as follows:

- $\Delta_{vs} = 50$ Hz: $t_c = 6.36$ ms
- $\Delta_{vs} = 5$ MHz: $t_c = 63.6$ ns

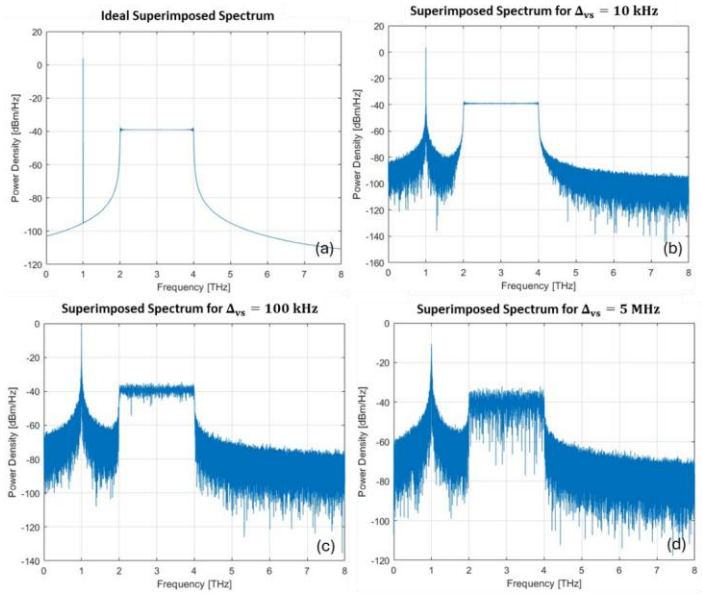

Figure 28. Spectrum of superimposed signal-static and swept laser-after the 3 dB coupler (a) in the absence of phase noise (b) for $\Delta_{vs} = 10$ kHz (c) for $\Delta_{vs} = 100$ kHz and (d) for $\Delta_{vs} = 5$ MHz

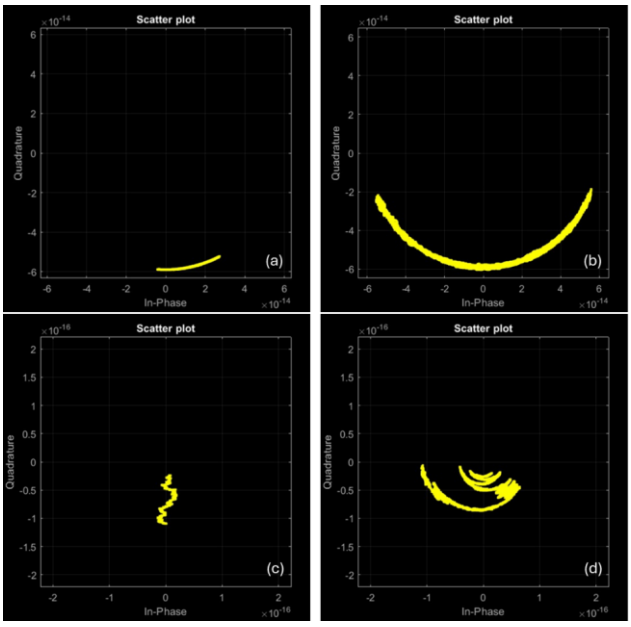

Figure 29. Indicative scatter plot of IF signal (a) for $\Delta_{vs} = 1$ MHz and (b) for $\Delta_{vs} = 25$ MHz neglecting FSPL and (c) for $\Delta_{vs} = 1$ MHz and (d) for $\Delta_{vs} = 25$ MHz when considering the FSPL

It is of interest to examine the effect of laser phase noise on the phase of the IF signal through a scatterplot of its in-phase and quadrature components. In the case where no envelope modulation is present in the sinusoidal signal, the phase noise results in a radial distribution of points in the scatterplot, as the amplitude remains constant. When taking into account the envelope modulation introduced by the THz attenuation, this distribution occurs around each distinct amplitude value. We therefore expect a pattern that can be described as a series of concentric circles, within each of which the radial phase noise is observed. These observations are illustrated in the following scatterplots, shown here for linewidths of 1 MHz and 25 MHz, respectively.

3.2 Calibration Algorithms

This section described the process of extracting the phase-voltage relationship for the heater based phase shifters of the two MZI meshes categories that will be employed in POLYNICES prototypes, hat is the Blass Matrix and the Clements Matrix. In subsection 3.2.1 a thoroughly description of the calibration process for the Blass Matrix is provided, while in subsection 3.2.2 the respective procedure for the Clements Matrix which follows the same rationale, is described more concisely.

3.2.1 Blass Matrix

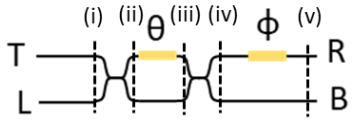

Figure 30. Tunable MZI with external phase shifter

Before proceeding to the analysis of the calibration process for a 4x4 Blass Matrix of Figure 29, it is essential to extract the equations for the output fields of a single MZI element with external phase shifter at the one of its output arms.

Point (i):

We assume that the input fields are coherent, and they can be expressed as follows:

$$E_{T,i} = |E_T| \cdot \exp(j \cdot \omega_c \cdot t) \tag{89}$$

$$E_{L,i} = |E_L| \cdot \exp(j \cdot \omega_c \cdot t) \tag{90}$$

where $|E_T|, |E_L|$ are the amplitudes of the input fields and ω_c is the carrier frequency.

Point (ii): At the output of the 3 dB beam splitter, the power of each field has decreased to one half, so the amplitude is weakened by the factor $\frac{1}{\sqrt{2}}$. Moreover, the waveguided field undergoes phase shift equal to $\frac{\pi}{2}$. Thus, the fields after the beam splitter are given as:

$$E_{T,ii} = \frac{E_{T,i}}{\sqrt{2}} + \frac{E_{L,i}}{\sqrt{2}} \cdot \exp\left(j \cdot \frac{\pi}{2}\right) \Rightarrow$$

$$E_{T,ii} = \frac{1}{\sqrt{2}} \cdot \left[E_T \cdot \exp(j \cdot \varphi) + E_L \cdot \exp\left(j \cdot \frac{\pi}{2}\right)\right] \tag{91}$$

$$E_{L,ii} = \frac{E_{T,i}}{\sqrt{2}} \cdot \exp\left(j \cdot \frac{\pi}{2}\right) + \frac{E_{L,i}}{\sqrt{2}} \Rightarrow$$

$$E_{L,ii} = \frac{1}{\sqrt{2}} \cdot \left[E_T \cdot \exp\left(j \cdot \left(\varphi + \frac{\pi}{2}\right)\right) + E_L\right] \tag{92}$$

Point (ii): At the output of the 3 dB beam splitter, the power of each field has decreased to one half, so the amplitude is weakened by the factor $\frac{1}{\sqrt{2}}$. Moreover, the waveguided field undergoes phase shift equal to $\frac{\pi}{2}$. Thus, the fields after the beam splitter are given as:

Point (iii): Then, the signal at the upper arm experiences phase shift equal to θ:

$$E_{T,iii} = E_{T,ii} \cdot \exp(j \cdot \theta) \Rightarrow$$

$$E_{T,iii} = \frac{1}{\sqrt{2}} \cdot \left[E_T \cdot \exp(j \cdot (\varphi + \theta)) + E_L \cdot \exp\left(j \cdot \left(\frac{\pi}{2} + \theta \right) \right) \right] \quad (93)$$

$$E_{L,iii} = E_{L,ii} \quad (94)$$

Point (iv): The field of the upper arm is subject to phase shift equal to φ. So, at point (i) before the beam splitter:

$$E_{T,iv} = E_T \cdot \exp(j \cdot \varphi) \quad (95)$$

$$E_{L,iv} = E_L \quad (96)$$

Output-Point (v): After the second 3 dB splitter, the fields at the two output ports of the MZI are equal to:

$$E_R = \frac{E_{T,iii}}{\sqrt{2}} + \frac{E_{L,iii}}{\sqrt{2}} \cdot \exp\left(j \cdot \frac{\pi}{2} \right) \Rightarrow$$

$$E_R = j \cdot \exp\left(j \cdot \frac{\theta}{2} \right) \cdot \left[E_T \cdot \sin\left(\frac{\theta}{2} \right) \cdot \exp(j \cdot \varphi) + E_L \cdot \cos\left(\frac{\theta}{2} \right) \right] \quad (97)$$

$$E_B = \frac{E_{T,iii}}{\sqrt{2}} \cdot \exp\left(j \cdot \frac{\pi}{2} \right) + \frac{E_{L,iii}}{\sqrt{2}} \Rightarrow$$

$$E_B = j \cdot \exp\left(j \cdot \frac{\theta}{2} \right) \cdot \left[E_T \cdot \cos\left(\frac{\theta}{2} \right) \cdot \exp(j \cdot \varphi) - E_L \cdot \sin\left(\frac{\theta}{2} \right) \right] \quad (98)$$

Now, we will distinguish some specific cases for the output fields, depending on the inputs and phases of internal and external phase shifters. We assume equal input amplitudes $|E|$ and zero initial phases.

Case 1: Two inputs and θ = π: The total input power is equal to the sum of the optical power of each fields:

$$P_{in} = P_T + P_L = 2 \cdot |E|^2 = 2 \cdot P \quad (99)$$

where $P = |E|^2$

In this case from (97) and (98) we get:

$$E_R = E \cdot \exp(j \cdot \pi) \cdot \exp(j \cdot \varphi) \quad (100)$$

$$E_B = E \quad (101)$$

The corresponding equations of output power are:

$$P_R = P_B = |E|^2 = \frac{P_{in}}{2} \quad (102)$$

So, the total input power is split between two outputs. The phases of the output fields differ by the amount $\varphi + \pi$. If we care only about the output power, we can set $\varphi = 0$.

Case 2: Two inputs and θ = 0: Again, the fields at the output ports have the same amplitude and their phases differ by φ. Also, they both experience $\frac{\pi}{2}$ phase shift, related to the input fields:

$$E_R = j \cdot E \tag{103}$$

$$E_B = j \cdot E \cdot \exp(j \cdot \varphi) \tag{104}$$

$$P_R = P_B = |E|^2 = \frac{P_{in}}{2} \tag{105}$$

If we set $\varphi = 0$, then the output fields have also the same phases.

Case 3: One input at the upper arm and $\theta = 0$: The total input power is equal to:

$$P_{in} = |E|^2 = P \tag{106}$$

The output fields are given as follows:

$$E_R = 0 \tag{107}$$

$$E_B = j \cdot E \cdot \exp(j \cdot \varphi) \tag{108}$$

and the corresponding power at each output:

$$P_R = 0 \tag{109}$$

$$P_B = |E|^2 = P_{in} \tag{110}$$

Thus, the power is "transferred" from the upper input arm to the lower output port (cross state) and the field experiences phase shift by $\varphi + \frac{\pi}{2}$. If the input field was at the lower arm, then for the cross state the power would be transferred to the upper output port with $\frac{\pi}{2}$ phase shift for the field.

Case 4: One input at the upper arm and $\theta = \pi$: The total input power is equal to:

$$P_{in} = |E|^2 = P \tag{111}$$

The output fields are given as follows:

$$E_R = -E \cdot \exp(j \cdot \varphi) \tag{112}$$

$$E_B = 0 \tag{113}$$

and the corresponding power at each output:

$$P_R = |E|^2 = P_{in} \tag{114}$$

$$P_B = 0 \tag{115}$$

In this case, the power is "transferred" from the upper input to the upper output (bar state) and the field experiences phase shift by $\varphi + \pi$. If the input field was at the lower arm, then for the bar state the power would be transferred to the lower output port without phase shift.

Case 5: Two inputs and $\theta = \pi/2$: In this case the total input power is:

$$P_{in} = P_T + P_L = 2 \cdot |E|^2 = 2 \cdot P \tag{116}$$

The fields at two output ports are given as follows:

$$E_R = j \cdot \exp\left(j \cdot \frac{3\pi}{4}\right) \cdot \left[\frac{E}{\sqrt{2}} \cdot \exp(j \cdot \varphi) + \frac{E}{\sqrt{2}}\right] \tag{117}$$

$$E_B = j \cdot \exp\left(j \cdot \frac{3\pi}{4}\right) \cdot \left[\frac{E}{\sqrt{2}} \cdot \exp(j \cdot \varphi) - \frac{E}{\sqrt{2}}\right] \tag{118}$$

In case $\varphi = 0$ the fields experiences phase shift by $\frac{3\pi}{4}$ and the input power is transferred at the upper output:

$$P_R = P_{in} \quad (119)$$

$$P_L = 0 \quad (120)$$

In case $\varphi = \pi$ the fields experiences phase shift by $-\frac{\pi}{4}$ and the input power is transferred at the lower output:

$$P_R = 0 \quad (121)$$

$$P_L = P_{in} \quad (122)$$

If the two input fields have phase difference equal to π, then the conditions for the power transfer are inversed.

Case 6: One input at upper arm and θ = π/2: In this case the total input power is:

$$P_{in} = P_T = P \quad (123)$$

The output fields can be expressed as:

$$E_R = j \cdot \exp\left(j \cdot \frac{\pi}{4}\right) \cdot \frac{E}{\sqrt{2}} \cdot \exp(j \cdot \varphi) \quad (124)$$

$$E_B = j \cdot \exp\left(j \cdot \frac{\pi}{4}\right) \cdot \frac{E}{\sqrt{2}} \cdot \exp(j \cdot \varphi) \quad (125)$$

So, the output signals have the same amplitude and phase shift equal to $\frac{3\pi}{4} + \varphi$, related to the input fields. The power is split between the two output branches:

$$P_R = P_B = \frac{|E|^2}{2} = \frac{P_{in}}{2} \quad (126)$$

Case 7: One input at lower arm and θ = π/2: Similar to the previous case, the power at each output port is:

$$P_R = P_B = \frac{P_{in}}{2} \quad (127)$$

What changes is that the phases of the output fields differ by π, as shown above:

$$E_R = j \cdot \exp\left(j \cdot \frac{\pi}{4}\right) \cdot \frac{E}{\sqrt{2}} \quad (128)$$

$$E_B = -j \cdot \exp\left(j \cdot \frac{\pi}{4}\right) \cdot \frac{E}{\sqrt{2}} \quad (129)$$

A useful conclusion from the above analysis, is that in case of one input or $\theta = 0$ or π (either one or two inputs), the external phase shifter does not affect the output power.

Regarding the induced phase shift to a heater-based phase shifter, it is proportional to the square of the applied voltage. Usually, in a practical realization there is also an initial offset resulting in not achieving the cross state for zero voltage or the bar state for the initial supposed V_{pi} voltage. This response, can be mathematically modelled as follows:

$$\theta = k_{theta} \cdot v_{theta}^2 + \theta_0 \quad (130)$$

where: k_{theta} is a constant and θ_0 is the initial phase offset.

Solving with respect to the voltage, it turns out that:

$$v_{theta}(\theta) = \sqrt{\frac{\theta - \theta_0}{k}} \quad (131)$$

Assuming a single input, the power to an output port of a single MZI, has a dependence only on the internal phase shift θ. We distinguish two cases:

- Signal enters the lower arm, and power is monitored to the upper arm, or vice versa:

$$P_{out} = \frac{P_{in}}{2} \cdot (1 + \cos\theta) \quad (132)$$

In this case, power is maximized for $\theta = 0$ or 2π and minimized for $\theta = \pi$.

- Signal enters the lower input arm and power is also monitored to the lower output arm (or respectively for the upper port):

$$P_{out} = \frac{P_{in}}{2} \cdot (1 - \cos\theta) \quad (133)$$

In this case, power is minimized for $\theta = 0$ or 2π and maximized for $\theta = \pi$.

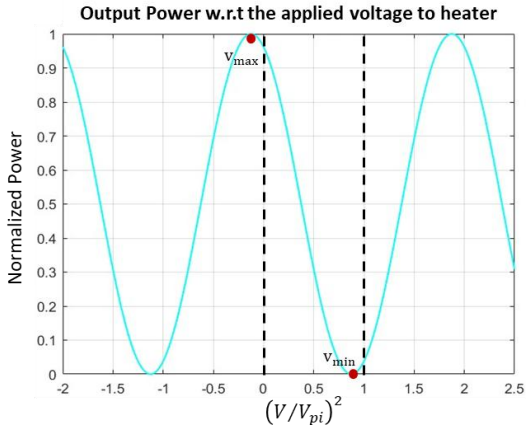

Figure 31. Normalized output power w.r.t the applied heater voltage for a top to bottom routing

In the above qualitive graph, the normalized output power $\left(\frac{P_{out}}{P_{in}}\right)$ as a function of the applied voltage squared (normalized with respect to an initial guessed V_{pi}^2) to the actuator is represented, for input at the top port and detection at the lower arm.

In an MZI mesh, the values of k and θ_0 differ from one MZI to another. For each one, we must extract these two parameters in order to precisely define the relationship (132). Having done that, we can calculate the required voltage for a desired phase shift and in turn configure the settings of the MZI mesh. In the below schematic, a 4x4 Blass Matrix architecture is depicted. The calibration process starts with the internal phase shifters. Every time light enters only one of the node's inputs and it is detected only from one of its outputs. In this case, as mentioned above, the value of φ does not

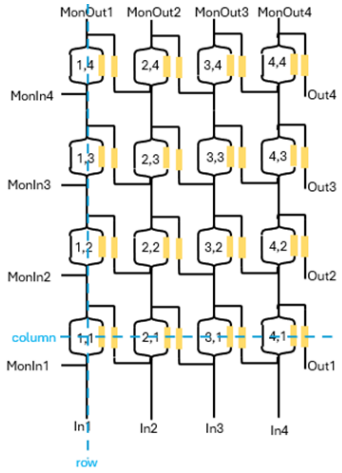

Figure 32. High level functional layout of a 4x4 Blass Matrix

matter, so we can calibrate the internal phase shifters without concern about variations in the external phase shifters.

The calibration starts from the first row. At each row, the MZIs are calibrated from last to first. The power is measured at the monitoring output which corresponds to the current row and light enters the monitoring input port at the row of the MZI being calibrated. In the current row, the already calibrated MZIs are set to cross state, in order to be someway "transparent" and route the optical field to the desired output. Similarly, the MZIs of the above row are also set to cross.

Following the described process, each MZI under calibration accepts light at the top port and routes it at the lower output port. Thus, equation (132) applies. We sweep the heater voltage to the maximum permittable range, in order to detect the minimum and maximum power. The voltage for which the power is maximized is equal to V_{cross} and the voltage that results in minimum power is equal to V_{bar}:

$$2 \cdot \pi = k \cdot V_{cross}^2 + \theta_0 \tag{134}$$

$$\pi = k \cdot V_{bar}^2 + \theta_0 \tag{135}$$

From the above equations, we can derive the unknown parameters as follows:

$$k = \frac{\pi}{V_{cross}^2 - V_{bar}^2} \tag{136}$$

$$\theta_0 = \frac{\pi \cdot V_{cross}^2}{V_{cross}^2 - V_{bar}^2} \tag{137}$$

The pseudocode of the calibration process for the internal phase shifters is given below.

```
N: number of rows
M: number of columns
n_cells: number of unit cells

Node_Isolation_theta(mesh,N,M,num_cells)

 for each row = 1 : N // calibrate each row from top to bottom
  out_idx -> row // detection port
  for col = M: -1 :1 // calibrate each node in the current row from last to
first
   in_idx -> col // monitoring input port
   calibrate_theta(mesh,row,col,in_idx,out_idx) // calibrate the current MZI
according to the min and max measured power
   set theta(row,col) = 0 // set calibrated node to cross
  end
  for k = 1 : M
   set theta(row,k) = 0 // after calibration, set the current row to cross
for the calibration of the next row
  end
 end

end


calibrate_theta(mesh,row,col,in_idx,out_idx)

 sweep voltage v_theta
  when P(v_theta) = min:
   v_theta = v_cross
  when P(v_theta) = max:
   v_theta = v_bar
  end

  k = π/(v_cross - v_bar)
  θ_0 = 2π - k*v_cross

end
```

Having calibrated the internal phase shifters, we can proceed to the calibration of the external phase shifters. For this purpose, both inputs must be "active" for each MZI. Additionally, the two input fields must be coherent with known and constant phase difference. In the proceedings, we assume that the two input fields are in phase. Also, for convenient purposes we consider the external phase shifter at the output branch of an MZI, as the external phase shifter of the input arm of the MZI at the above row.

For a single MZI with two inputs and $\theta = \frac{\pi}{2}$, the detected power at the upper output arm is given by:

$$P_R = P_{in} \cdot \left(1 + \cos(\varphi)\right) \tag{138}$$

As a result, power is maximized for $\varphi = 0$ or 2π and minimized for $\varphi = \pi$.

The calibration starts from the 2nd row, and the two optical fields are injected to the current and previous row. The node at the same column and previous row is at the bar state in order to route the optical field from their bottom input port to the top input port of the node being calibrated. Bar state from bottom to bottom does not induce phase shift. All the other nodes of the current and previous row are set to cross, and power is measured at the monitoring output port of the current row. Propagation through an MZI at cross state, causes a phase difference of $\frac{\pi}{2}$. However, the optical fields

from the input ports of the mesh till the input ports of the MZI being calibrated, pass through the same number of MZIs at cross state, so their initial phase difference is not affected.

The internal phase shift of the current MZI is set to $\frac{\pi}{2}$ and the heater voltage is swept in order to find the arguments of min and max power. So according to equation (138), maximum power is measured for V_{cross} and minimum power is measured for V_{bar}:

$$k_{phi} = \frac{\pi}{V_{cross}^2 - V_{bar}^2} \tag{139}$$

$$\varphi_0 = \frac{\pi \cdot V_{cross}^2}{V_{cross}^2 - V_{bar}^2} \tag{140}$$

After calibration, the external phase shift of the node is set to 0. The corresponding pseudocode is presented below.

```
Node_Isolation_phi(mesh,N,M,num_cells)

  for each row = 1 : N
   in_idx -> row - 1, row // optical fields at the main input ports of
current and previous row
   out_idx - > row // detection port
   for each col = 1 : M
    theta(row,col) = π/2 // set the internal PS of the current MZI to π/2
    theta(row-1,col) = π // set the above node to bar
    theta(row-1,j) = 0 for j != col // set all the other nodes of the
previous row to cross
    theta(row,j) = 0 for j != col // set the other nodes of the current row
to cross
    calibrate_phi(mesh,row,col,in_idx,out_idx) // calibrate the current MZI
according to the min and max measured power
    phi(row,col) = 0 // after calibration set phi to zero
    theta(row,col) = 0
  end
 end

end

calibrate_phi(mesh,row,col,in_idx,out_idx)

 sweep voltage: v_phi
  when P(v_phi) = min:
   v_theta = v_bar
  when P(v_theta) = max:
   v_theta = v_cross
 end

  k = π/(v_cross - v_bar)
θ_0 = 2π - k*v_cross
 end
```

Example 1

Input field: at In1

$\theta_{(1,1)} = \frac{\pi}{2}$

$\theta_{(2,1),(3,1),(4,1)} = 0$

$\theta_{(1,2)} = \pi$

$\theta_{(2,2),(3,2),(4,2)} = 0$

The input optical field at In1 is equally split in the two output arms of $MZI_{(1,1)}$. Then the power is routed at the main output ports 1 and 2 through the 1st and 2nd columns.

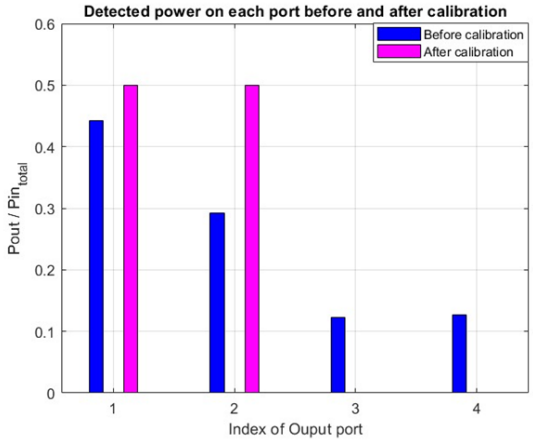

Figure 33. Output power normalized to input power before and after theta calibration for Example 1

Example 2

Input field: at In4

$\theta_{(4,1),(4,2),(4,3)} = 0$

$\theta_{(4,4)} = \pi$

The input field at In4 is propagated to the upper input arm of $MZI_{(4,4)}$, through $MZIs_{(4,1),(4,2),(4,3)}$. Then, $MZI_{(4,4)}$ routes the optical power to Out4.

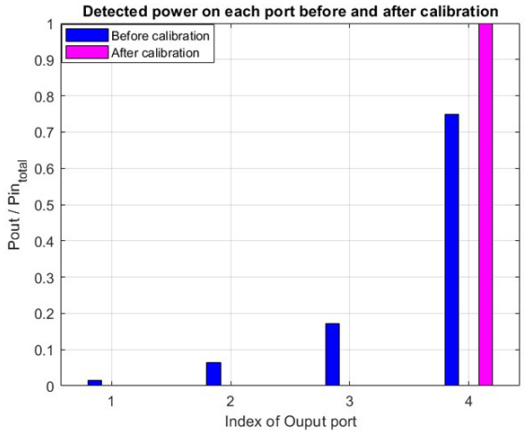

Figure 34. Output power normalized to input power before and after theta calibration for Example 2

Example 3

Input fields: at In1 and In2

$\theta_{(1,1)} = \pi$

$\theta_{(2,1)} = \pi/2$

$\varphi_{(2,1)} = 0$

$\theta_{(2,2)} = \pi$

$\theta_{(3,2),(4,2)} = 0$

The total input power is routed through $MZI_{(2,1)}$ at the input of $MZI_{(2,2)}$. Then, $MZIs_{(3,2),(4,2)}$ direct the power to Out2.

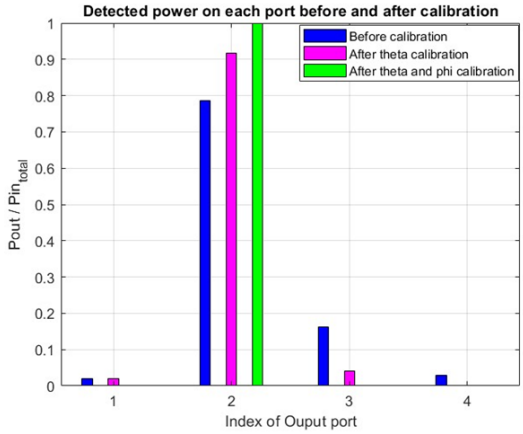

Figure 35. Output Power before and after theta and phi calibration for Example 3

Example 4

Input fields: at In1 and In4

$\theta_{(2,1)} = 0$

$\theta_{(2,2)} = \pi$

$\theta_{(4,1),(4,2)} = \pi/2$

$\varphi_{(4,2)} = 0$

$\theta_{(4,3)} = \pi$

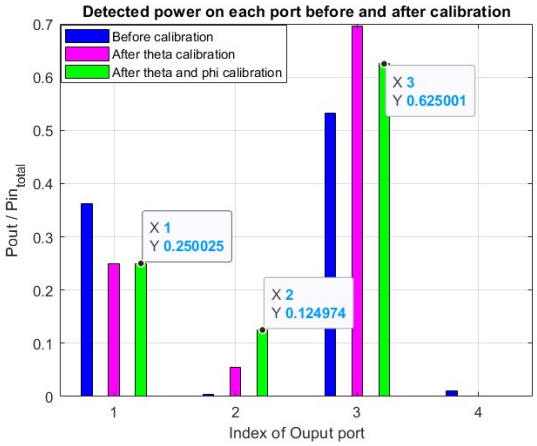

Figure 36. Output Power before and after theta and phi calibration for Example 4

Then the power distribution at the main output ports of the Blass Matrix is as follows:

$$\begin{cases} P_{out,1} = \dfrac{P_{in,tot}}{4} \\ P_{out,2} = \dfrac{P_{intot}}{8} \\ P_{out,3} = \dfrac{5 \cdot P_{intot}}{8} \end{cases} \tag{141}$$

In the following the explanation of the above result is given.

For $MZI_{(4,1)}$ we have a single input at the lower arm and $\theta = \frac{\pi}{2}$. Thus:

$$E_{out(4,1),up} = \exp\left(j\frac{3\pi}{4}\right) \cdot \frac{E}{\sqrt{2}} \tag{142}$$

$$E_{out(4,1),low} = -\exp\left(j\frac{3\pi}{4}\right) \cdot \frac{E}{\sqrt{2}} \tag{143}$$

where E: is the amplitude of the input fields. This field is the lower input of $MZI_{(4,2)}$:

$$E_{out(4,1),up} = E_{in(4,2),low} \tag{144}$$

The optical field of input 2, propagated through two MZIs at cross state ($MZIs_{(2,1),(3,2)}$) and one MZI at bar state ($MZI_{(2,2)}$) bottom to bottom until the lower input port of $MZI_{(4,2)}$. So the optical amplitude remains E and the induced phase change is equal to:

$$\Delta\varphi = 2 \cdot \frac{\pi}{2}\ (\text{cross}) + 1 \cdot 0\ (\text{bar} - \ \text{bottom to bottom}) = \pi \tag{145}$$

Thus, at the upper branch of $MZI_{(4,2)}$, the optical field is equal to:

$$E_{in(4,2),up} = -E \tag{146}$$

The applied phase shift to $MZI_{(4,2)}$ is $\frac{\pi}{2}$. As a result:

$$E_{out2} = E_{out(4,2),low} = -\exp\left(j\frac{3\pi}{4}\right)\cdot\left[\frac{E}{\sqrt{2}} + \frac{E}{\sqrt{2}}\cdot\exp\left(j\frac{3\pi}{4}\right)\cdot\frac{1}{\sqrt{2}}\right] = -\exp\left(j\frac{3\pi}{4}\right)\cdot\frac{E}{\sqrt{2}}\cdot\left[1+\exp\left(j\frac{3\pi}{4}\right)\cdot\frac{1}{\sqrt{2}}\right] \quad (147)$$

The optical field of the upper output of $MZI_{(4,2)}$ is propagated to Out3 through $MZI_{(4,3)}$ at bar state from bottom to bottom. So:

$$E_{out3} = E_{out(4,2),up} = -\exp\left(j\frac{3\pi}{4}\right)\cdot\left[\frac{E}{\sqrt{2}} - \frac{E}{\sqrt{2}}\cdot\exp\left(j\frac{3\pi}{4}\right)\cdot\frac{1}{\sqrt{2}}\right] = -\exp\left(j\frac{3\pi}{4}\right)\cdot\frac{E}{\sqrt{2}}\cdot\left[1-\exp\left(j\frac{3\pi}{4}\right)\cdot\frac{1}{\sqrt{2}}\right] \quad (148)$$

Having defined the output optical fields, we can calculate the corresponding optical powers:

$$P_{out1} = E_{out(4,1),low} = \left(\frac{E}{\sqrt{2}}\right)^2 = \frac{E^2}{2} = \frac{P_{in,tot}}{4} \quad (149)$$

$$P_{out2} = \frac{E^2}{2}\cdot\left|1+\exp\left(j\frac{3\pi}{4}\right)\cdot\frac{1}{\sqrt{2}}\right|^2 = \frac{P_{in,tot}}{4}\cdot\left(1-2\cdot\frac{\cos\left(\frac{3\pi}{4}\right)}{\sqrt{2}}+\frac{1}{2}\right) = \frac{P_{in,tot}}{8} \quad (150)$$

$$P_{out3} = \frac{E^2}{2}\cdot\left|1-\exp\left(j\frac{3\pi}{4}\right)\cdot\frac{1}{\sqrt{2}}\right|^2 = \frac{P_{in,tot}}{4}\cdot\left(1+2\cdot\frac{\cos\left(\frac{3\pi}{4}\right)}{\sqrt{2}}+\frac{1}{2}\right) = \frac{5\cdot P_{in,tot}}{8} \quad (151)$$

where:

$$P_{in,tot} = 2\cdot E^2 \quad (152)$$

3.2.2 Clements Matrix

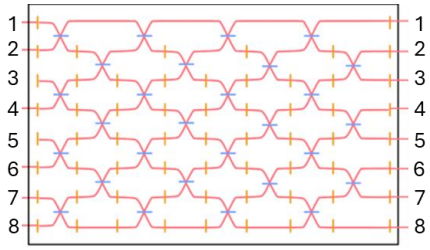

Figure 37. Schematic diagram of 8x8 Clements Matrix

The calibration of internal phase shifters of the MZIs included in the 8x8 Clements Matrix will be based on equations (132) or (133). In relation to the phase shifters at the input arms of the MZI's, the calibration requires coherent light of the same amplitude entering both inputs. In this case, if we set the internal phase shift of the MZI at $\theta = \frac{\pi}{2}$ then the detected power at the top and bottom output port respectively equals to:

$$P_{up} = P_{in}\cdot[1+\cos(\Delta\varphi)] \quad (153)$$

$$P_{low} = P_{in}\cdot[1-\cos(\Delta\varphi)] \quad (154)$$

where φ the applied phase shift at the top input arm, φ' the applied phase shift at the lower input arm and $\Delta\varphi = \varphi - \varphi'$. Thus, only the relationship of the phase difference with the applied voltage can be extracted. Due to this fact, we can extract the relationships when sweeping the voltage to the one phase shift while applying zero voltage to the other.

For the internal phase shifters calibration, light enters only one of the node's inputs and it is detected only from one of its outputs. In this case, as mentioned above, the value of $\Delta\varphi$ does not matter, so we can calibrate the internal phase shifters without concerning about variations in the external phase shifters. An additional step which must be implemented is the definition of the sequence of nodes for calibration. This definition will be based on the "Node Isolation Algorithm" [5], which will be described consciously in the following. We start with the calibration of the main diagonal. Light is inputted in In_1 and detected in the last photodetector, in our case at Out_8. The nodes through the main diagonal are calibrated from bottom to top and each node is set to cross state. Then, the top of the mesh can be calibrated, one diagonal layer at a time, starting with the layer above the main diagonal. Each diagonal is calibrated, using a different PD and input In_1, by isolating and calibrating one node at a time from bottom to top. For the first top diagonal, if $\mathrm{N} = \mathrm{M}$, where M is the number of columns and N the number of rows, then we use $\mathrm{Out}_{\mathrm{N}-1}$ for detection, else we use $\mathrm{Out}_{\mathrm{N}-2}$. In our case, we use Out_6. Then, for each following top diagonal we proceed with step -2 regarding the output used for detection. While calibrating each top diagonal:

- The node being calibrated is set to bar state in order to direct the field to the current detector: light enters the lower input of the current MZI and exits from the lower output
- All other nodes in the same diagonal are set to cross
- The node being at the main diagonal one row below the current node is set to bar and all other nodes of the main diagonal are set to cross
- The remaining nodes are set to bar state

Finally, the bottom of the mesh can be calibrated one diagonal layer at a time, starting with the layer directly below the main diagonal. Light inputs into In_3 and for each subsequent diagonal, the input number increases by two. Each diagonal is calibrated by isolating and calibrating one node at a time, from the top down, by setting already calibrated nodes to a bar state, except for those on the current diagonal, which are set to cross state. Also, the node being calibrated is set to bar state in order to direct the field to the current detector: light enters the upper input of the current MZI and exits from the upper output. A node at row i, is calibrated through Out_i. During this activity an external LS can be employed.

After the calibration of internal phase shifters, we can calibrate the external phase shifters. For this purpose, we should shine coherent light into both the input ports of the MZI under investigation. Thus, it is essential to utilize the phase-locked ECLs of the laser sub-module of Demo 2A. We start from the first column, and we move to the last with step equal to 1. For each column, we calibrate the MZIs from top to bottom.

- First, we set $\theta_{\mathrm{i,j}} = 0$ and we shine coherent light into each input
- For each column:
  I. We set all the internal PS to $\frac{\pi}{2}$
  II. For each row i, we calibrate φ using the output with index i
  III. We set φ = 0 to the calibrated phase shifters
  IV. We reset MZIs to cross state ($\theta_{\mathrm{i,j}} = \pi$)

As we shine light into all inputs and at the same time the MZIs are set to cross state (except from those to the column being calibrated), all the MZIs of the following columns receive power in both their input arms. For an MZI being calibrated, $\theta = \frac{\pi}{2}$. Thus, if the two inputs are in phase, the power is maximized at the current output for $\varphi = 0$, because Out_i is on the same row as the upper output arm

Commented [EL1]: Alexiev, C., Mak, J. C. C., Sacher, W. D., & Poon, J. K. S. (2021). Calibrating rectangular interferometer meshes with external photodetectors. *OSA Continuum*, *4*(11), 2892. https://doi.org/10.1364/osac.437918

of $MZI_{(i,j)}$. On the contrary, for phase difference equal to π the detected power is maximized for $\varphi = \pi$. In the following we present some indicative examples from the simulation results. In the first two cases, only the state of internal phase shifters concerns us, because each MZI either receives power at only one input port or is set at bar or cross state.

Example 1

Input field: at In1

$\theta_{(1,1)-(7,7)} = 0$

In this case, light enters from the first input port and travels through the main diagonal of the Clements Matrix to the last output port.

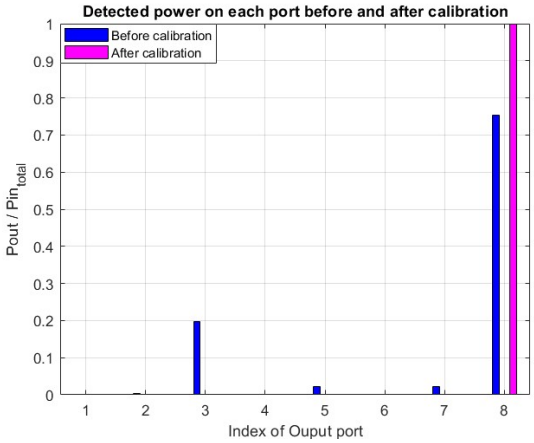

Figure 38. Output Power before and after theta calibration for Example 1

Example 2

Input field: at In4

$\theta_{(3,1)} = \pi$

$\theta_{(6,8)} = \pi/2$

$\theta_{else} = 0$

In this example, the power is transferred from the bottom input port of $MZI_{(3,1)}$ to its lower output port. Then, by setting all the MZIs of the corresponding diagonal at cross state, it is routed to the lower input port of $MZI_{(7,7)}$ which is also at cross state. Thus, the input power has been transferred to the lower input port $MZI_{(6,8)}$ and from there it is equally split to the output ports 6 and 7, by setting the internal phase shifter of $MZI_{(6,8)}$ at π/2.

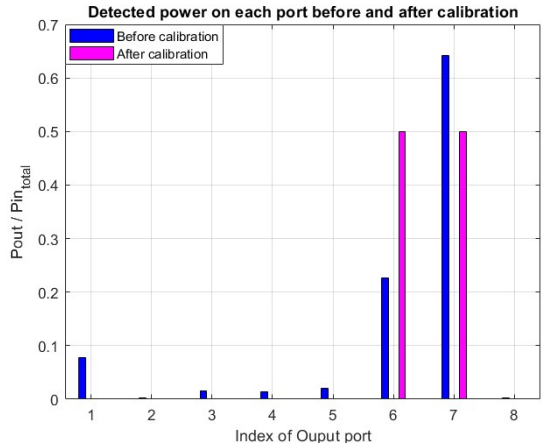

Figure 39. Output Power before and after theta calibration for Example 2

Example 3

Input field: at In7 and In8

$\varphi = 0$ (for all the MZIs)

$\theta_{(7,1),(6,2)} = \pi/2$

$\theta_{else} = \pi$

The power is transferred from the last two input ports (7 and 8) to the upper output port of $MZI_{(7,1)}$. Then, $MZI_{(6,2)}$ receives power at its lower input port and its internal phase shifter is set at $\pi/2$, thus the input power is equally split at its two output ports. The proceeding MZIs are set at bar state, so the power is finally transferred at output ports 6 and 7, with the same ratio.

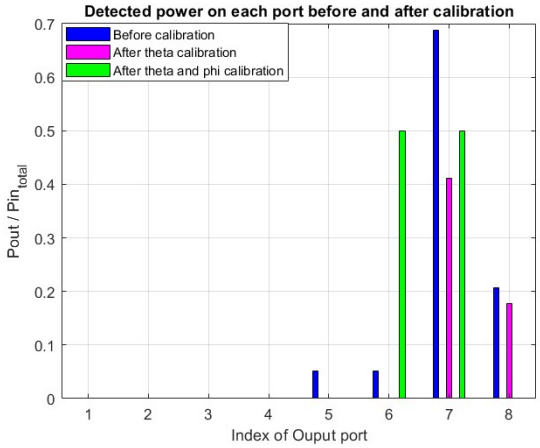

Figure 40. Output Power before and after theta and phi calibration for Example 3

4 CONCLUSIONS

For the family of the FMCW THz spectrometers, five (5) prototypes will be designed and fabricated. Three of them (**Precursor-0A, Precursor-1A**, **Precursor-1B**) are precursor prototypes that will pave the way for the development of the two main prototypes (**Demo-1A** and **Demo-1B**). More specifically, **Precursor-0A** is a high-power external cavity laser source operating in the C-band. It will comprise a InP RSOA as gain medium and a TriPleX waveguide circuit as external cavity. The RSOA is edge-coupled to the external cavity. Two coupled MRRs with slightly different FSRs in the cavity will ensure stable single frequency operation due to the Vernier effect. **Precursor-1A** is THz transmitter and receiver that will be designed and fabricated utilizing the POLYNICES integration approach. Using an EOPCB as the host platform, both the InP elements and the silicon rod antennas will be integrated, enabling the emission and detection of THz signal. The prototypes will be designed to support the operation with THz signals with frequencies above 1 THz. **Demo-1A** will be a single channel FMCW THz spectrometer and it will be the first main prototype of this family of prototype. **Demo-1A** will utilize the POLYNICES EOPCB platform and will consist of a high-power dual-laser source, a pair of THz antennas and a wavelength locker. **Precursor-1B** will include an 4×4 OBFN based on the Blass matrix architecture combined with a carrier insertion stage and an array of 4 THz transmitters and 2 THz receivers. **Demo-1B** is the final prototype of the FMCW THz spectrometer family and the most sophisticated from the system point of view. Following a systematic and step-wise approach, **Demo-1B** will build upon all the previous prototypes of the same family to demonstrate a multi-channel FMCW THz spectrometer. Demo-1B will consist of a high-power dual-laser source and an 4×4 OBFN based on the Blass matrix architecture combined with a carrier insertion stage and an array of 4 THz transmitters and 2 THz receivers.

For the family of the quantum information processors, three (3) prototypes will be designed and fabricated. **Precursor-2A** will be a fiber-pigtailed ppKTP crystal integrated on PolyBoard alongside with polarization handling elements to sperate the signal and idle. **Demo-2A** will be an integrated squeezed light state source based on KTP crystals and a 8x8 Clements matrix. It will consist of three units; the laser units that will host four phase-locked high power laser sources, operating at 775 nm, the ppKTP unit and the quantum information processor unit that will host four ppKTP crystals, polarization handling elements, a pump suppression unit and a 8x8 Clements matrices, respectively. **Demo-2B** will be an integrated squeezed light state source based on micro-ring resonators and a 8x8 Clements matrix. It will consist of a photon-generating unit, a pump suppression and filtering unit as well as an 8x8 Clements matrix.

The studies presented in this deliverable will play a pivotal role in guiding and streamlining the upcoming testing phase. Together with the simulation studies reported in Deliverable D2.2, they provide detailed insights into component-level performance, system-level behavior, and calibration strategies, thereby establishing a robust framework for experimental validation. The comprehensive simulation results, combined with the refined specifications, will enable targeted verification of critical functionalities, support the early identification of potential issues, and ultimately accelerate the integration and optimization of the final prototypes.

List of Figures

List of Tables

References

[1] https://www.hhi.fraunhofer.de/fileadmin/PDF/PC/HYB/20181009-Micro-Optical-Bench-web.pdf

[2] Marpaung, D., Roeloffzen, C., Heideman, R., Leinse, A., Sales, S., & Capmany, J. (2013). Integrated microwave photonics. Laser & Photonics Reviews, 7(4), 506–538. https://doi.org/10.1002/lpor.201200032